AGU PUBLICATIONS

JGR

Journal of Geophysical Research: Solid Earth

RESEARCH ARTICLE
10.1002/2017JB014867

Key Points:
- We develop boundary element models of fault-related folding of viscoelastic layers embedded with a reverse fault
- Buckling by flexural slip can dramatically amplify fault-related folds
- Strength of bedding contacts, thickness and stiffness of layering, and fault geometry all contribute significantly to fold form

Correspondence to:
K. M. Johnson,
kajjohns@indiana.edu

Citation:
Johnson, K. M. (2018). Growth of fault-cored anticlines by flexural slip folding: Analysis by boundary element modeling. *Journal of Geophysical Research: Solid Earth*, *123*, 2426–2447. https://doi.org/10.1002/2017JB014867

Received 14 AUG 2017
Accepted 16 FEB 2018
Accepted article online 21 FEB 2018
Published online 11 MAR 2018

Growth of Fault-Cored Anticlines by Flexural Slip Folding: Analysis by Boundary Element Modeling

Kaj M. Johnson[1]

[1]Department of Earth and Atmospheric Sciences, Indiana University, Bloomington, IN, USA

Abstract Fault-related folds develop due to a combination of slip on the associated fault and distributed deformation off the fault. Under conditions that are sufficient for sedimentary layering to act as a stack of mechanical layers with contact slip, buckling can dramatically amplify the folding process. We develop boundary element models of fault-related folding of viscoelastic layers embedded with a reverse fault to examine the influence of such layering on fold growth. The strength of bedding contacts, the thickness and stiffness of layering, and fault geometry all contribute significantly to the resulting fold form. Frictional contact strength between layers controls the degree of localization of slip within fold limbs; high contact friction in relatively thin bedding tends to localize bedding slip within narrow kink bands on fold limbs, and low contact friction tends to produce widespread bedding slip and concentric fold form. Straight ramp faults tend to produce symmetric folds, whereas listric faults tend to produce asymmetric folds with short forelimbs and longer backlimbs. Fault-related buckle folds grow exponentially with time under steady loading rates. At early stages of folding, fold growth is largely attributed to slip on the fault, but as the fold increases amplitude, a larger portion of the fold growth is attributed to distributed slip across bedding contacts on the limbs of the fold. An important implication for geologic and earthquake studies is that not all surface deformation associated with blind reverse faults may be attributed to slip on the fault during earthquakes.

1. Introduction

Blind faults underlying actively growing anticlines are a significant seismic hazard globally, affecting heavily populated areas including Japan (e.g., Ishiyama et al., 2004; Sugiyama et al., 2003), Los Angeles (e.g., Shaw et al., 2002), and western Taiwan (e.g., Yue et al., 2011). Quantifying the hazard associated with blind reverse faults is not straightforward because fault slip often does not reach the ground surface and slip on the fault must be inferred indirectly. Figure 1 shows subsurface data from two active anticlines in southern and central California, which illustrate the difficulty of identifying the deep seismogenic fault and relating it to the shallower fold geometry. Reverse-faulting earthquakes occurred under the Santa Fe Springs Anticline in the 1987 Whittier Narrows earthquake in Los Angeles (Figure 1a; Shaw et al., 2002), and the 1983 Coalinga earthquake ruptured a blind fault underlying the Coalinga Anticline in central California (Figure 1b; Guzofski et al., 2007). While the surface and shallow (<5 km) geometry of the anticlines are well established from geology and subsurface borehole and reflection data, the earthquakes ruptured at much greater depths of 10–13 km on faults that are not well imaged. As is the case here, it is often not entirely clear how the shallow geometry of fault-cored anticlines relates to the underlying seismogenic fault. In practice, blind fault geometry and estimates of slip rates on the blind faults need to be inferred indirectly through fault-related fold models.

Another challenge is that very few large earthquakes on blind faults coring anticlines have been recorded with modern geodetic observations. A few studies utilizing geodetic measurements of coseismic surface deformation document growth of anticlines over blind faults as a consequence of slip on faults during moderate-sized earthquakes. Stein and King (1984) and Stein and Ekström (1992) proposed that folds at Coalinga and Kettleman Hills California form by growth during repeated earthquakes on blind reverse faults. Stein and King (1984) established this idea based on the similarity in pattern between vertical displacements determined from leveling measurements before and after the 1983 Coalinga earthquake and deformed river terraces. Belabbès et al. (2009) used interferometric synthetic aperture radar (InSAR) to document coseismic uplift of the Berdani fold in Algeria due to slip on a blind fault in a Mw 5.7 earthquake. Tizzani et al. (2013) and Pezzo et al. (2013) used InSAR data and deformation modeling to show that coseismic uplift of anticlinal structures in the northern Appennines frontal thrust system in Italy can be attributed to slip on blind faults underlying the folds in a sequence of Ml = 5.9 and Ml = 5.8 earthquakes in 2012. Nissen et al. (2007) used

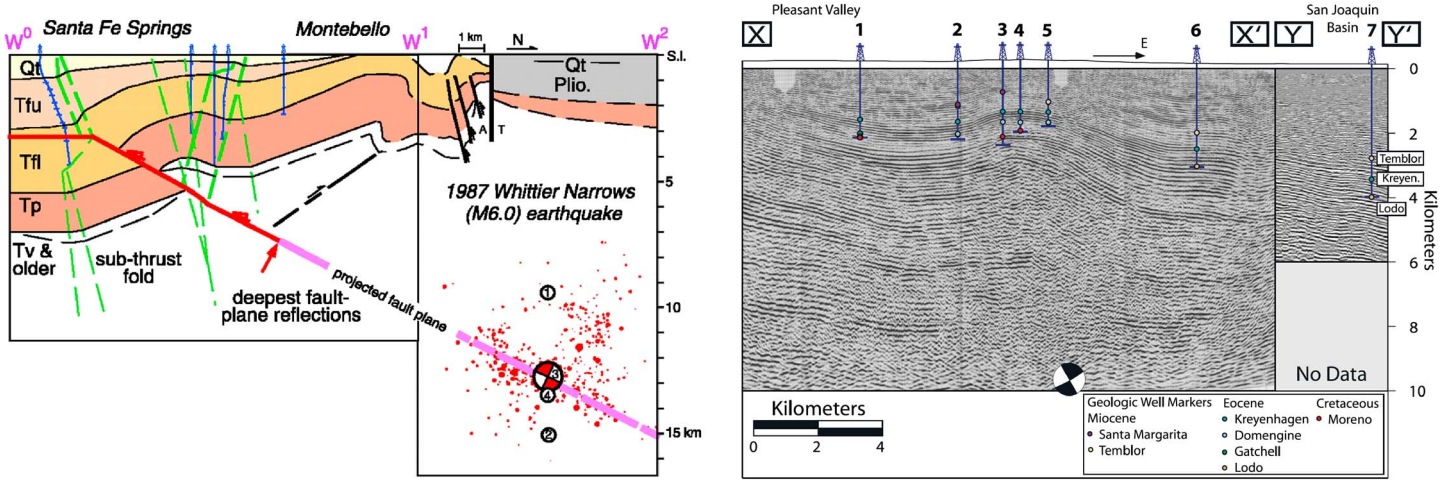

Figure 1. Two examples of fault-cored anticlines over active blind faults that have ruptured recently in M6–7 earthquakes. (a) Santa Fe Springs Anticline in Los Angeles (Shaw et al., 2002). (b) Coalinga Anticline in central California (Guzofski et al., 2007).

InSAR to record coseismic uplift centered on a major anticline in the Zagros Simply Folded Belt due to the 2005 Mw 6 Qeshm Island earthquake. Geodetic data for each of these events were modeled with slip on buried faults in an elastic medium.

It has become a nearly universal assumption in the literature that crustal-scale anticlines grow primarily by slip on underlying faults and fold geometry and uplift rate of active fault-related folds can be used directly to infer the fault slip rate from an assumed kinematic relationship (e.g., Suppe, 1983). For example, Grant et al. (1999) used dates from uplifted marine terraces in the San Joaquin Hills, California, to infer slip rate on underlying blind reverse faults, assuming that the uplift rates are directly related to the total slip rate through the sine of the dip angles of the faults. Ishiyama et al. (2004) mapped and dated uplifted alluvial terraces on the active Kuwana anticline in central Japan to obtain estimates of uplift rate. They assumed a kinematic relationship between the uplifted terrace surfaces and an underlying fault to infer the fault slip rate. Shaw et al. (2002) used the method of Shaw and Suppe (1994), based on kinematic constructions of fold-growth structures, to infer fault slip rates and to assess size and frequency of future earthquakes on the Puente Hills blind thrust fault, which ruptured in the 1987 Whittier Narrows earthquake under metropolitan Los Angeles. Allmendinger and Shaw (2000) used the trishear kinematic model to infer the total amount of fault slip on the thrust underlying the Puente Hills. The geodetic studies discussed in the previous paragraph also assume that coseismic fold growth is directly related to slip on the underlying fault.

On the other hand, it is recognized in the literature that fold growth can be accommodated without slip on a causative fault. Several studies have inferred distributed shortening off of the main fault. Veloza et al. (2015) used geomorphic and seismic data from the active Tame Anticline in the eastern Colombia Subandes to infer that ~40% of total finite shortening of the anticline occurs as distributed off-fault deformation. It is also known that distributed strain is a significant component of shortening at the scale of a fold and thrust belt, with distributed deformation locally accounting for 10–50% of the total shortening (e.g., Duebendorfer & Meyer, 2002; Hogan & Dunne, 2001; Mitra, 1994; Yonkee & Weil, 2010). Detachment folds are thought to grow by distributed pure shear above a detachment surface, without a ramp fault coring the uplift (e.g., Gonzalez-Mieres & Suppe, 2006; Poblet & McClay, 1996). Theoretically, buckle folds can grow in amplitude without a fault. For example, the theory of folding of initial perturbations in isolated layers or multilayers without faulting is well established (e.g., M. A. Biot, 1961; M. Biot, 1964; Chapple, 1969; Fletcher, 1977; A. M. Johnson & Fletcher, 1994). In this theory of folding, buckling is accommodated either by flexural slip at layer contacts or through flexural flow within interbeds. However, as discussed in more detail below, mechanical analyses of fault-related folding have largely focused on passive folding by slip on faults; the mechanical layers required for buckle folding are absent in many analyses. Notable exceptions are the numerical

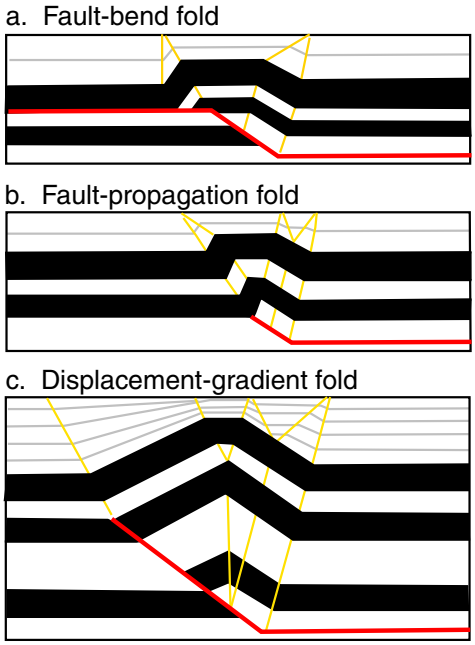

Figure 2. Three kinematic constructions of idealized fault-related folds considered in this study. The gray lines denote growth strata, and the alternating black and white layers denote pregrowth strata. The yellow lines are axial traces. (a) Fault-bend folds form as rock is translated through bends in fault. (b) Fault-propagation folds form as a result of a bend in the fault and termination of slip at the fault tip. (c) Displacement-gradient folds form as a result of a nonpropagating fault tip and tapering of slip toward the tip.

simulations of Shackleton and Cooke (2007) and Albertz and Lingrey (2012) and analogue experiments of Bonanno et al. (2017) that showed that folding of layers above a blind fault is enhanced by allowing flexural slip at layer contacts.

The purpose of this paper is to examine the growth of fault-cored anticlines through the coupled processes of fault slip and flexural-slip folding. We develop a boundary element model of the growth of an anticline over a fault embedded in a medium with viscoelastic layers that slip at frictional contacts. We show that not only does the fault geometry influence fold shape but the thickness of folded layers and the frictional strength at layer contacts all have a first-order impact on the shape of fault-related folds. We further show that fault-cored anticlines may not grow strictly by the mechanism of fault slip, but that folds in a mechanically layered medium can be significantly amplified by buckling under horizontal compression with a significant portion of shortening being distributed through the fold.

2. Kinematics and Mechanics of Fault-Cored Anticlines

Two broad classes of fault-cored folds that we consider in this study are fault-bend folds and fault-tip or fault-propagation folds (Figure 2). Fault-bend folds form when rock moves through a flat-ramp-flat fault geometry and generates a ramp anticline (e.g., Suppe, 1983). Fault propagation and fault-tip folds form by distributed deformation ahead of the terminations of propagating or nonpropagating reverse faults. A number of kinematic models, similar to the Suppe (1983) construction, have been devised to capture the basic geometry of fault-tip and fault-propagation folds (e.g., Chester & Chester, 1990; Suppe & Medwedeff, 1990). Figure 2c shows the displacement-gradient fold geometry of Wickham (1995) in which slip on the ramp fault tapers to zero at the tip. The trishear kinematic model (e.g., Erslev, 1991) produces rounded fold forms by assuming distributed shear in a triangular wedge in front of the propagating fault tip. Brandes and Tanner (2014) provide a recent review of the most popular kinematic folding models from the literature.

Mechanical theories for ramp folding in homogenous linear elastic or viscous media without layer interfaces have been developed previously (e.g., A. M. Johnson & Berger, 1989; Berger & Johnson, 1982; Johnson & Fletcher, 1994; Kilsdonk & Fletcher, 1989; Savage & Cooke, 2003; Wiltschko, 1979). None of these analyses consider the buckling mechanism through flexural slip between layers. Similarly, mechanical models of faulting in media without layer interfaces have been developed for forced-folds (e.g., K. M. Johnson & Johnson, 2002; Patton & Fletcher, 1995; Ze'ev Reches & Johnson, 1978) and fault-propagation folds (e.g., Cardozo et al., 2003, 2005; Finch et al., 2003). Again, each of these mechanical models investigates the passive folding of markers in materials of various rheology in response to slip on a fault. On the other hand, boundary element models of Cooke and Pollard (1997); finite element analyses by Niño et al. (1998), Sanz et al. (2008), and Albertz and Lingrey (2012); and analogue experiments by Bonanno et al. (2017) examined the influence of slip between bedding planes in fault-related folding. These studies show that the existence a few layers with interface slip can significantly influence the resulting shape of the fold. However, the fault was not embedded within layering in any of these studies and flexural slip was limited to a few slip surfaces.

Huang and Johnson (2016) developed boundary element models to examine the growth of folds over blind faults in a layered elastic medium with free slip at layer contacts. They showed that the fold grows through the combined mechanisms of fault slip and buckling of layers and that the fold in a layered medium can grow to more than twice the amplitude of a fold without layering. The purpose of the current study is to extend the Huang and Johnson (2016) analysis to buckle folding in a viscoelastic layered medium accommodated by flexural slip along frictional bedding contacts. In the next sections, we review what is known from the literature about buckle folding and the role of frictional bedding contacts on fold form.

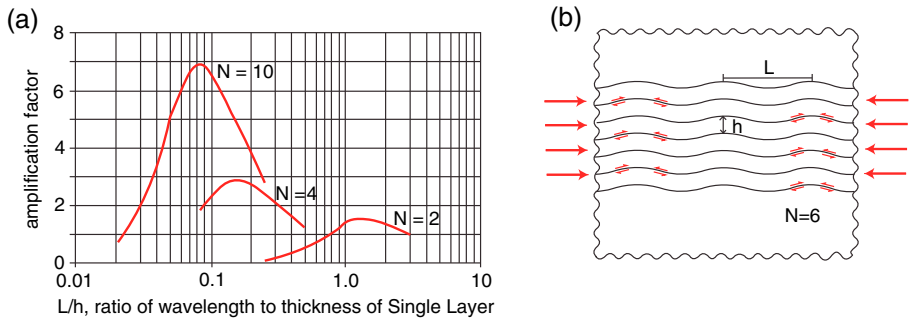

Figure 3. Illustration of amplification factor from viscous folding theory of A. M. Johnson and Pfaff (1989). (a) Amplification factor plotted as a function of wavelength of perturbation normalized by layer thickness. *N* is number of layers. (b) Illustration of wavelength, layer thickness, and loading condition.

2.1. Amplification of Folding by Flexural-Slip Buckling

A number of theoretical studies of multilayer folding have investigated the process of amplification of initially small perturbations (e.g., Biot, 1964; Chapple, 1969; Fletcher, 1977; Johnson & Fletcher, 1994; Mancktelow, 1999). The rate at which an initial perturbation is amplified in linear materials is a function of the number of layers in the multilayer, *N*, thickness of layers, *h*, and initial perturbation wavelength, *L* (Figure 3b). The rate at which initial sinusoidal perturbations grow in amplitude under horizontal shortening was quantified by Biot (1961) and Fletcher (1977) as the "amplification factor" (e.g., Johnson & Fletcher, 1994).

Figure 3 shows the amplification factor as a function of the wavelength of the perturbation normalized by the layer thickness for layers with viscosity equal to the surrounding media and free slip at layer contacts using the theory described by A. M. Johnson and Pfaff (1989) for folding of linear viscous layers. The amplification factor is shown for multilayers with $N = 2$, 4, and 10. Figure 3 illustrates that the amplification factor increases with the number of layers, *N*. Also, for a given layer thickness and number of layers, there is a "dominant wavelength" for which the amplification factor is largest (the peak of the curves). Thus, Figure 3 demonstrates the rather intuitive result that very broad or very narrow initial perturbations, relative to the thickness of the layers, grow in amplitude more slowly than perturbations with a dominant wavelength and perturbations in a multilayer with many thin layers grow in amplitude more quickly than in a multilayer of the same total thickness but composed of a few thick layers.

The concept of amplification factor is relevant in a general way to fault-cored folding in a multilayer under layer-parallel shortening. In this case, we anticipate that the wavelength of the initial perturbation produced by slip on the fault would be controlled by the dip and length of the underlying fault. As in free folding, we anticipate the rate of amplification of the fold to be controlled by the shortening rate and the thickness and number of layers. A fault-cored fold in a medium without layering is expected to grow more slowly than a fold overlying a fault in a medium with many mechanical layers. Huang and Johnson (2016) indeed showed that folding of an elastic multilayer with free slip at layer contacts above a reverse fault is amplified significantly by buckling. Folds produced within relatively thin layering (layers several times thinner than the wavelength) can grow to 4–5 times the amplitude of a fold in a medium without layering. Amplification through flexural slip folding was also noted by Shackleton and Cooke (2007).

2.2. Flexural Slip and Fold Geometry

Experimental studies of folding of elastic multilayers by, for example, Cobbold (1976) and Honea and Johnson (1976) demonstrate that fold form is strongly influenced by contact strength. Figures 4a and 4b illustrate two end-member cases of experimental folding by Honea and Johnson (1976) of photoelastic rubber strips subjected to layer-parallel shortening where the experimental conditions are identical except for contact strength. Figure 4a shows rounded, concentric folds within layers lubricated at contacts with silicone grease (low frictional resistance to slip). Figure 4b shows sharp-hinged, localized conjugate kink folds in layers with dry contacts (high frictional resistance to slip). Figure 4c, from Reches and Johnson (1976), shows monoclinal kink folds in layers with dry contacts subjected to additional shear parallel to layering. The facing direction of the kink bands is opposite to the sense of imposed layer-parallel shear. A theory of kink folding and the

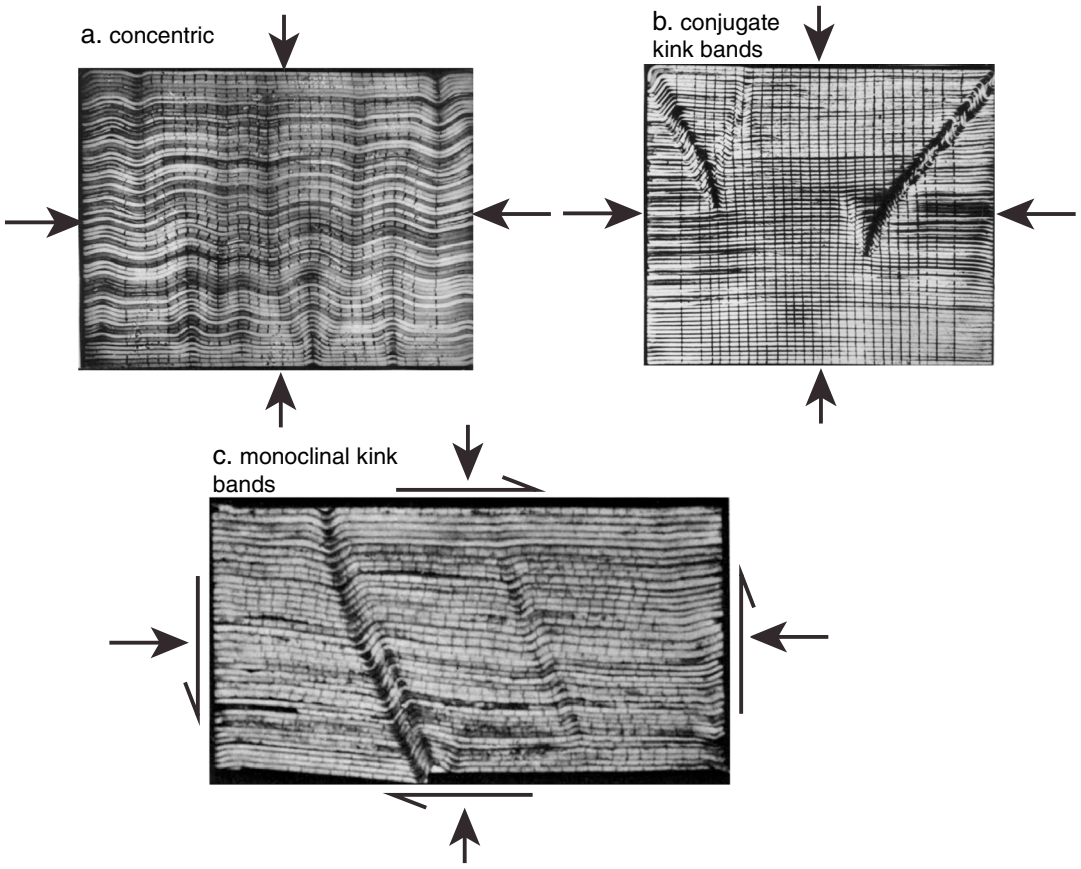

Figure 4. Experimental folding of photoelastic rubber strips from (a and b) Honea and Johnson (1976) and (c) Reches and Johnson (1976). Stack of rubber strips subjected to layer-parallel shortening with vertical confinement. (a) Contacts lubricated with silicone grease. Repeated concentric folds are formed under low frictional contact. (b) Dry, frictional contacts. Isolated left- and right-facing conjugate kink bands form. (c) Dry, frictional contacts. Additional shear is imposed. Isolated left-facing monoclonal kink bands form.

influence of contact strength on fold form was developed for elastic layers by Honea and Johnson (1976) and Reches and Johnson (1976) and viscous layers by Pfaff and Johnson (1989). As in the experimental folds, the primary ingredient in the theoretical analyses for transition from rounded, concentric folds to sharp-hinged, localized kink folds is nonlinear contact strength (such as friction or cohesion).

3. Boundary Element Analysis of Flexural Slip

To investigate the growth of fault-cored anticlines by flexural slip folding, we have developed a boundary element model, Boundary Element Analysis of Flexural Slip (BEAFS). We model a fault embedded in a multilayer consisting of viscoelastic layers within frictional contact (Figure 5). The fault and layers are embedded in a viscoelastic halfspace. Ramp-flat faulting is modeled with a lower horizontal flat that connects to a ramp fault. The ramp fault either terminates at the top (fault-tip folding) or connects to an upper flat (fault-bend folding). Steady slip is imposed on the flat(s). The initial stress state before slip or far-field loads are imposed is assumed to be lithostatic (pressure increasing linearly with depth). An additional arbitrary horizontal far-field stress, σ_{ff}, may also be imposed to represent a tectonic load as well as a vertical load to represent water loading for the case of submarine deformation ($\sigma_w = 0$ in all simulations in this study). We model rock as a persistently fractured viscoelastic material. We assume that the rock contains numerous fractures such that the instantaneous, elastic response of the rock can be approximated as an elastic material with effective stiffness lower than that of the intact rock. Kemeny and Cook (1986) used principles of linear elastic fracture mechanics to show that an elastic solid containing a random distribution of interacting cracks can be approximated by representing the elastic moduli of the solid with effective moduli and a crack density parameter.

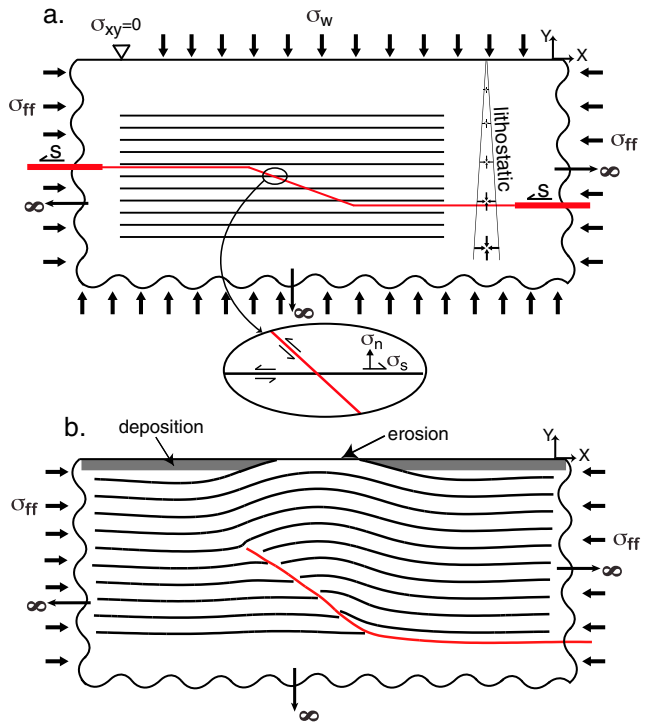

Figure 5. Illustration of geometry and boundary conditions. (a) Ramp-flat folding drive by slip, *s*, on a lower and (optionally) upper flat. Initial far-field horizontal tectonic load, σ_{ff}, and vertical water load, σ_w, can be imposed. Pressure is assumed to be lithostatic. Normal, σ_n, and shear, σ_s, tractions are resolved on faults and layer contacts. (b) Illustration of treatment of deposition and erosion. Ground surface is always flat. All material above surface is eroded, and deposition fills subsiding regions.

Generally, it has been shown in the rock mechanics literature that the effective elastic Young's modulus, *E*, and shear modulus, *G*, of a fractured elastic solid can be represented as

$$\frac{1}{E} = \frac{1}{E_0} + \frac{1}{k_n S}$$
$$\frac{1}{G} = \frac{1}{G_0} + \frac{1}{k_s S}, \tag{1}$$

where *S* is fracture spacing and k_n and k_s are normal and shear fracture stiffness parameters, respectively. E_0 and G_0 are the elastic moduli of intact rock between fractures. We further assume that over time the rock relaxes stress as a linear viscous material. Thus, we assume a linear Maxwell viscoelastic material that is parameterized by an effective elastic shear modulus, *G*, and Poisson's ratio, ν, and viscosity, η.

Faults and layer contacts assigned a coefficient of friction, μ_f. The layers and the fault are assumed to slip according to a cohesionless Coulomb friction law, $|\tau_s| \leq \mu_f \sigma_n$, where τ_s is shear stress and σ_n is normal stress (compression is positive). The fault does not propagate mechanically; however, we examine the influence of kinematically propagating the fault tip in section 9 of this paper.

As illustrated in Figure 5b, erosion and deposition are treated very simply. We assume a uniform deposition rate. Material that moves above the free surface is assumed to erode to maintain a flat free surface. There is no attempt to balance deposited and eroded mass.

We expand on the elastic displacement discontinuity method of Crouch and Starfield (1983) and discretize the fault surfaces and layer contacts using the solution for plane-strain edge dislocations in a viscoelastic halfspace. This is an extension of the purely elastic boundary element formulation as described by Huang and Johnson (2016) that assumed frictionless contacts. The solution for a dislocation in a viscoelastic halfspace is easily obtained from the dislocation solution in an elastic halfspace using the correspondence principle of viscoelasticity (e.g., Segall, 2010). A similar approach was adopted by Huang and Johnson (2012) to develop viscoelastic models of interseismic strain accumulation across strike-slip faults.

We adopt a Maxwell viscoelastic material with governing equation

$$\dot{\sigma}_{ij} + \frac{\mu}{\eta}\left(\sigma_{ij} - \frac{\sigma_{kk}}{3}\delta_{ij}\right) = 2\mu\dot{\epsilon}_{ij} + \lambda\dot{\epsilon}_{kk}\delta_{ij}, \tag{2}$$

where λ and μ are the usual elastic Lamé constants, the dots denote time derivative, and repeated indices indicate summation. Segall (2010) gives the expression for displacements and stresses for an edge dislocation in an elastic halfspace. The detailed expressions are not repeated here as the relationship of displacements and stresses to elastic moduli is the only relevant part of the relationship for this explanation. The stresses are of the form

$$\sigma_{ij} = \frac{\mu}{(1-\nu)} f_{ij}, \tag{3}$$

where the f_{ij} are functions of the geometry and dislocation magnitude only (not elastic parameters). Thus, applying the correspondence principal of viscoelasticity, the stresses have the simple form in the Laplace domain,

$$\overline{\sigma}_{ij}(s) = \frac{\overline{\mu}(s)}{(1-\overline{\nu}(s))} f_{ij}, \tag{4}$$

where

$$\overline{\mu}(s) = \frac{\mu s}{s + \mu/n}, \overline{\nu}(s) = \frac{1}{2}\frac{\lambda s + K\mu/n}{(\mu+\lambda)s + K\mu/\eta} \tag{5}$$

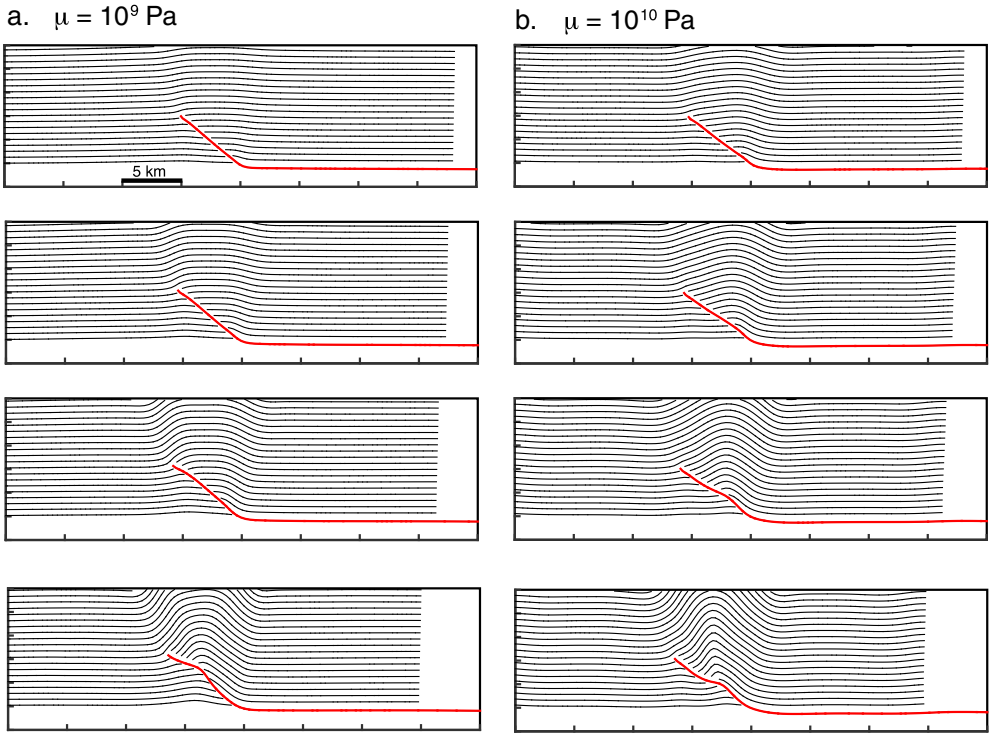

Figure 6. (a and b) Influence of elastic stiffness on fold form. $\sigma_{xx} = 10^7$ Pa and $\mu_f = 0.4$. See text for more details on conditions. Simulation conditions in (a) and (b) differ only in elastic stiffness. Amount of slip on the flat increases from top to bottom.

and K is elastic bulk modulus and s is the transform domain variable. In this study, we take the special case of an incompressible elastic material such that $\nu \rightarrow \frac{1}{2}$. In this case, $\overline{\nu}(s) \rightarrow \frac{1}{2}$ since $+\lambda \rightarrow \lambda$. The inverse Laplace transform of stress (3) gives stress in the time domain,

$$\sigma_{ij}(t) = e^{-\frac{\mu}{\eta}t} f_{ij}. \tag{6}$$

The stresses simply decay exponentially with characteristic time, η/μ. The displacements in an elastic halfspace are a function of Poisson's ratio, but not μ. Thus, again assuming elastic incompressibility, the displacements in the viscoelastic halfspace are independent of time.

We discretize faults and layers into straight displacement discontinuity elements. We also discretize time into equal time steps. Assume we have an $N \times 1$ vector of incremental values of the dip component of slip at the jth time increment, s^j, on N elements. From the solution for a 2-D edge dislocation and solution for decaying stress (6), we construct the $N \times N$ matrices, $\boldsymbol{G}_s$ and $\boldsymbol{G}_n$, that relate vectors of shear stresses, σ_s^j, and normal stresses, σ_n^j, at the center of each element during time step j to slip on all the elements at time steps 1,2, …, $j-1$ as

$$\sigma_s^j = \sum_{k=1}^{j-1} G_s^k s^k, \quad \sigma_n^j = \sum_{k=1}^{j-1} G_n^k s^k. \tag{7}$$

We define the vectors of shear and normal stresses at centers of all N elements due to an increment of imposed slip on the lower flat (and upper, if it exists) as $\boldsymbol{\sigma}_s^d$ and $\boldsymbol{\sigma}_n^d$, respectively. We also define the vector of normal stresses at centers of all N elements due to lithostatic load, σ^L, and the vectors of shear and normal stresses due to far-field horizontal stress, $\boldsymbol{\sigma}_s^{ff}$ and $\boldsymbol{\sigma}_n^{ff}$. Assuming a coefficient of friction, μ_f, on all elements, at the jth increment of deformation we iteratively solve for the distribution of slip, s_j, on elements to satisfy the Coulomb friction condition,

$$\left|\boldsymbol{\sigma}_s^{ff} + \boldsymbol{\sigma}_s^j + G_s^j s_j\right| \le \mu_f \left(\boldsymbol{\sigma}_n^{ff} + \sigma^L + \boldsymbol{\sigma}_n^j + G_n^j s_j\right), \tag{8}$$

which requires the shear stress on patches (left side) not exceed the frictional strength (right).

4. Influence of Rheology on Fold Form

We begin our analysis by examining the influence of stiffness and viscosity on folding. Figure 6 shows the result of folding of an elastic multilayer (no viscous relaxation) with a 45° dipping ramp fault above a horizontal flat. Both sets of simulations assume all conditions are the same except for the effective elastic shear modulus. The contact friction is $\mu_f = 0.4$, initial horizontal stress is $\sigma_{xx} = 10^7$ Pa, the deposition rate at the surface is zero, and a uniform density of $\rho = 3$ g/cm^3 is assumed. Seismically-determined elastic shear moduli in the crust are of order 10 GPa. In Figure 6 we compare folds for the case of a relatively soft effective shear modulus, $\mu = 10^9$ Pa, with folding using a higher shear modulus corresponding closer with seismically determined values, $\mu = 10^{10}$ Pa. It is clear from Figure 6 that the fold form depends on elastic stiffness. In the softer layering, kink bands form the forelimb and backlimb of a symmetric fold with a relatively flat crest. In the stiffer layering, kink bands do not form, but rather the fold form is quite rounded at all stages of folding and is slightly asymmetric in the earlier stages of folding with a longer forelimb and shorter backlimb. The reason for the lack of kink bands in the stiffer layering is that the imposed differential stresses from slip on the flat are large enough to overcome frictional contact strength throughout the fold and allow pervasive interlayer slip. In the softer layering, the imposed differential stresses due to slip on the flat are an order of magnitude lower per increment of shortening and contact strength is overcome only locally, on the limbs of the folds, which encourages the development of kink bands.

Figure 7 shows viscoelastic layer simulations with varying viscosity. All other conditions are identical to simulations shown in Figure 6a. We show the result for various viscous relaxation times, $t_R = \eta/\mu$, for fixed slip rate, $\dot{s}$, on the flat, or equivalently, different slip rates for fixed viscous relaxation times. If the amount of slip occurring over a characteristic relaxation time is large, that is, $\dot{s} * t_R \gg 1$ (Figure 7d), the layering is effectively elastic because the relaxation process is slow relative to the loading rate. As the amount of slip over a characteristic relaxation time ($\dot{s} * t_R$) decreases, the relaxation process is fast relative to the loading rate, and stress relaxation through viscous flow becomes more important. This can be seen in Figure 7, where the folding is increasingly suppressed with decreasing viscosity (shorter relaxation times). In the case of Figure 7a, the relaxation time is so short relative to the loading rate that there is very little flexural-slip buckling; the fold grows largely by distributed viscous flow throughout the medium surrounding the fault. In contrast, the fold grows rapidly through flexural-slip buckling in the effectively elastic case (Figure 7d).

It is difficult to assess realistic viscous relaxation times for the crust because it is not clear what actual physical relaxation process in the crust the linear viscosity might represent. For the sake of assigning some numbers to these parameters, let us assume that the dominant relaxation mechanism in the crust is pressure solution creep of calcite and/or quartz. As shown by Rutter and Elliott (1976), the creep law for pressure solution can be approximated as linear viscous flow. Gratier et al. (1999) developed a brittle-ductile creep law for pressure solution in the upper crust assuming the linear creep formulation of Rutter and Elliott (1976) that gives an average pressure solution creep viscosity of 3×10^{21} Pa s. We can get a conservative range of possible viscosities from quartz and calcite deformation mechanism maps of Rutter and Elliott (1976). For 10–1,000 μm sized calcite grains below 200°C (corresponding to depths shallower than 10 km for a typical geotherm), predicted pressure solution strain rates at differential stresses of 0.1–100 MPa range from 10^{-12} to 10^{-15} s^{-1}, giving allowable viscosities of 10^{19}–10^{21} Pa s. For 10–1,000 μm sized quartz grains, the allowable range of viscosities is 10^{20}–10^{24} Pa s. For comparison, there are at least two studies in which penetrative strain rates of upper crustal rocks have been estimated in compressional deformation belts. Gratier and Gamond (1990) used the study of McEwen (1978) on deformation of alpine molassic conglomerates to infer strain rates of order 10^{-14}–10^{-15} s^{-1}. Duebendorfer and Meyer (2002) inferred penetrative strains in rocks above 10 km depth in the Ventura basin of southern California of 17–27% during contractional deformation over 3–5 million years. This gives strain rates of 1–3 $\times$ 10^{-15} s^{-1}. Assuming deviatoric stresses of order 1–100 MPa, the viscosity would be of order 10^{20}–10^{23} Pa s. Returning to Figure 7, we assumed an elastic shear modulus of 10^9 Pa, so $\dot{s} * t_R = 0.32$ km for a slip rate of 10 mm/yr gives a viscosity of 10^{21} Pa s. At a slip rate of 10 mm/year the $\dot{s} * t_R \gg 1$ km case in Figure 7d corresponds to a viscosity of greater than about 10^{22} Pa s, the $\dot{s} * t_R = 1$ km case in Figure 7c corresponds to a viscosity of about 3×10^{21} Pa s, and the $\dot{s} * t_R = 0.1$ km case in Figure 7a corresponds to a viscosity of about 3×10^{20} Pa s.

We see from Figure 7 that while the viscosity of the medium influences that rate of buckle folding, the resulting fold geometry is not strongly influenced. Clearly, buckle folding is maximized for the high-viscosity

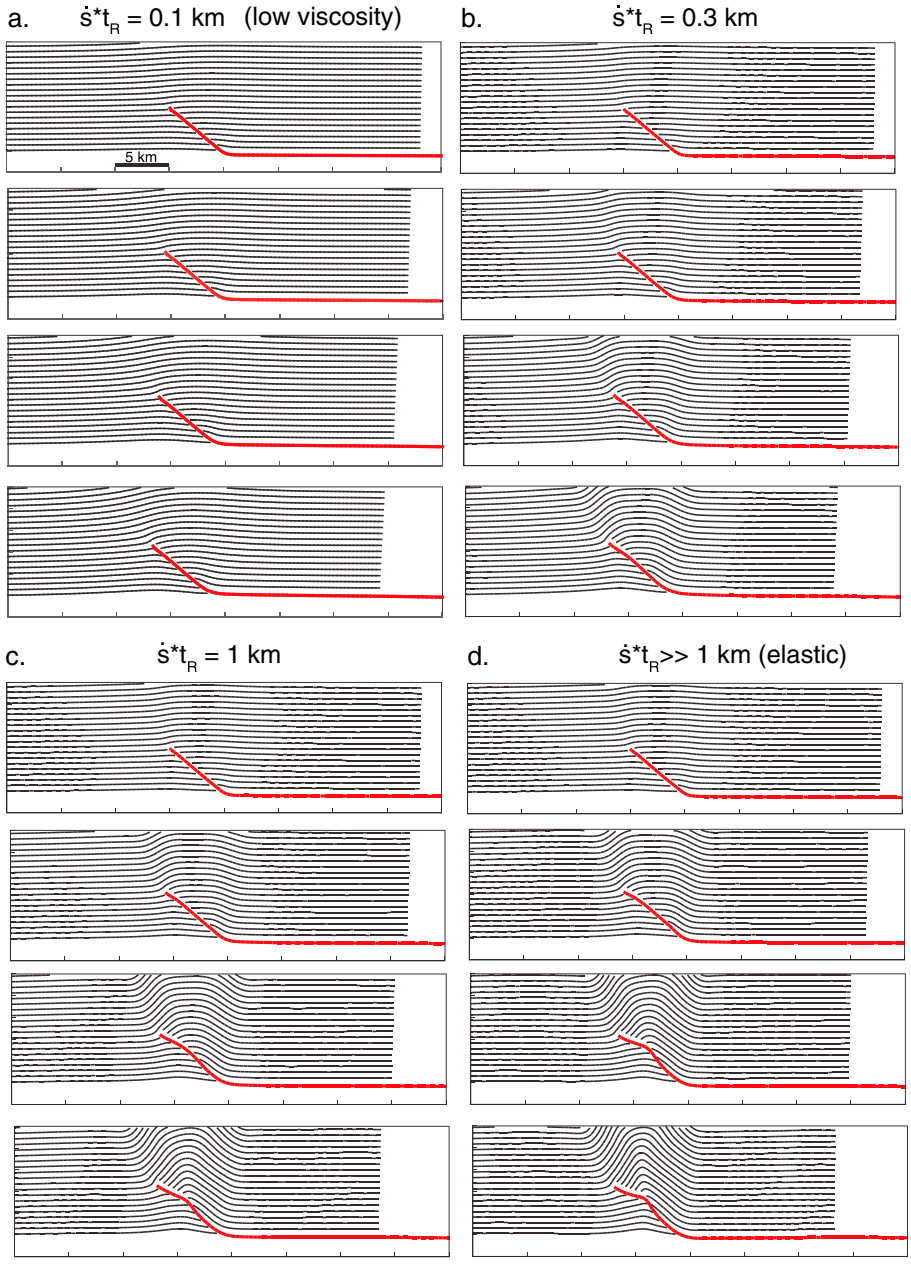

Figure 7. Influence of viscosity on fold form. Conditions are identical to that of Figure 6a except for viscosity. Here t_R is relaxation time of viscoelastic layers and $\dot{s}$ is slip rate on the flat. Thus, $\dot{s} * t_R$ is the amount of slip on the flat occurring over the characteristic relaxation time.

(effectively elastic) case. In all of the following simulations in this paper, we will assume $\dot{s} * t_R \gg 1$ km such that relaxation can be neglected.

5. Contact Strength and Fold Form

We begin our analysis of contact strength on fold form by examining the case of folding of an elastic multilayer without a fault. The purpose of this analysis is to illustrate the influence of contact strength on fold form, which was analyzed with analytical folding theory for viscous materials by Johnson and Pfaff (1989) and Pfaff and Johnson (1989). Figure 8 shows the result of shortening a stack of elastic layers embedded in an elastic medium. The layers resubjected to uniform initial confining stresses. In the case of Figure 8c, the medium is

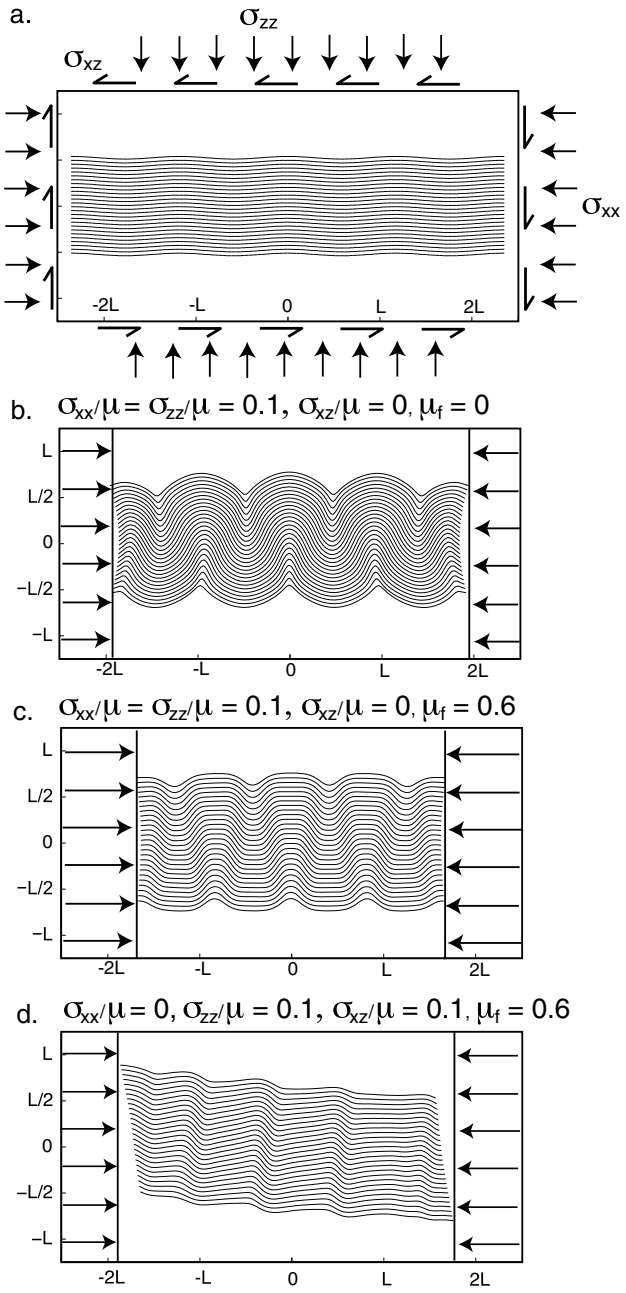

Figure 8. Boundary element simulations of multilayer folding under horizontal shortening and uniform initial confining pressure. (a) Boundary conditions and initial low-amplitude sinusoidal perturbation of layering. (b) Free slip at layer contacts under horizontal shortening. (c) Frictional contacts under horizontal shortening. (d) Frictional contacts with nonzero initial shear stress (layering becomes inclined to horizontal shortening direction).

also subjected to initial shear stress, σ_{xz}. Here we do not have a flat fault to impose loading, so instead we subject the entire medium to increments of horizontal shortening by imposing far field incremental strains, ϵ_{xx} and $\epsilon_{zz} = -\nu\epsilon_{xx}/(1-\nu)$. A sinusoidal initial perturbation is assigned to the layers as illustrated in Figure 8a. The result depends only on ratios of stress to rigidity. For these simulations, we have chosen confining stress ratios of $\sigma_{xx}/\mu = \sigma_{zz}/\mu = 0.1$, but similar results are obtained for ratios down to about 0.01. Figure 8b shows the nearly concentric form that results from the case of free slip (zero friction) at layer contacts under the illustrated stress conditions. The fold form is similar to the third-order analytical form demonstrated by Johnson and Pfaff (1989) for the case of linear viscous layers of uniform viscosity with free slip embedded in a viscous medium. The conditions of folding here are similar to the conditions giving concentric folds in the physical experiments of rubber strips shown in Figure 4a.

Figure 8c shows conjugate kink folds under the condition of frictional contacts, similar to that observed in the physical rubber strip experiments shown in Figure 4b. The loading conditions in Figure 8c are identical to that in Figure 8b except for the contact strength. Figure 8d shows that monoclonal kink folds with a single facing direction form when the layering is subjected to layer-parallel shear. The conditions in Figure 8d are the same as Figure 8c except that an initial shear stress, σ_{xz}, is imposed such that the layering becomes inclined to the horizontal compression. The fold asymmetry produced here is similar to the geometry in the physical experiments (Figure 4c) and the theoretical analysis by Pfaff and Johnson (1989).

The point of this analysis was to show that the boundary element models reproduce an important result expected from physical experiments and theoretical studies: fold form strongly depends on the nature of contact strength between layers. Fold form can vary from rounded, concentric forms with zero contact strength to kinked, localized folding with frictional strength (or more generally, nonlinear contact strength as demonstrated by Pfaff and Johnson, 1989). Furthermore, conjugate kink folds displaying both left- and right-facing limbs form under layer-parallel shortening, and monoclinal kink folds with a single facing direction form when layering is inclined to shortening.

We now examine the influence of layer contact strength on fault-related fold geometry. Figure 9 shows four simulations in which the conditions are identical except that contact friction is varied. The viscosity is high such that layers are effectively elastic with shear modulus of 10^9 Pa. The initial horizontal stress is $\sigma_{xx} = 10^7$ Pa, the deposition rate at the surface is zero, and density is $\rho = 3$ g/cm^3. The consequence of frictional strength is similar to that for free folding (Figure 8). For free slip (zero contact friction), the resulting fold is rounded and nearly concentric in form at early folding stages. At later stages, the fold becomes asymmetric. With lower to moderate friction ($\mu_f = 0.2$–0.6), kink bands form at the fault tip and fault bend, resulting in a flat-top fold geometry. In the case of bonded contacts (Figure 8d), there is no buckling and the fold is diffuse. The explanation for the rounded fold form for free slip and the kink-band geometry for the moderate friction cases is clear from examination of Figure 10, which shows the incremental slip on the fault and at layer contacts (in km) for the case of free slip and $\mu_f = 0.6$. Free slip encourages widespread flexural slip, whereas frictional contacts encourage slip to localize into kink bands.

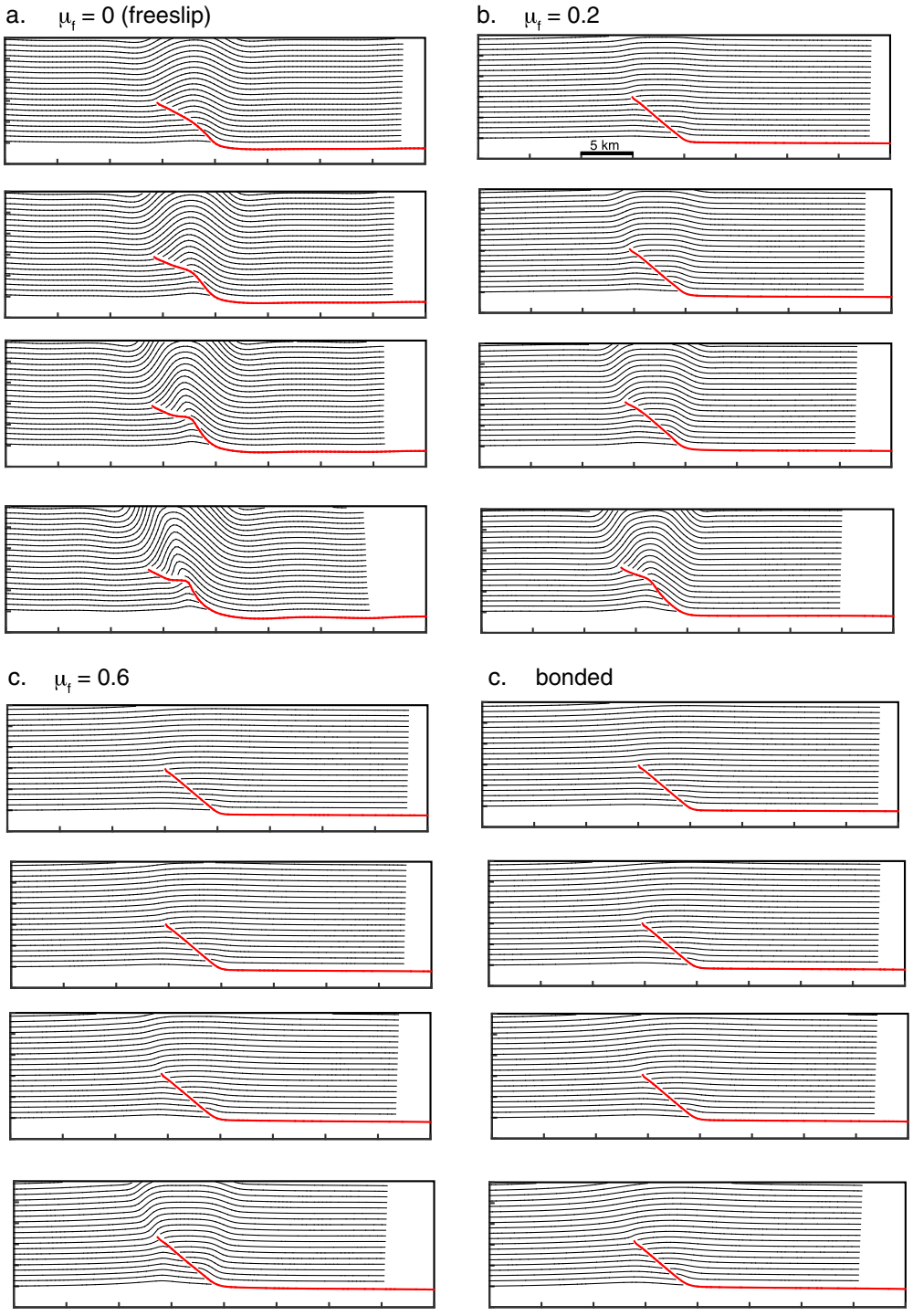

Figure 9. Role of layer contact friction on fold form. All conditions except contact friction are the same in each simulation. High viscosity case (effectively elastic layers). Shear modulus is 10^9 Pa, initial horizontal stress $\sigma_{xx} = 10^7$ Pa, the deposition rate at the surface is zero, and density is $\rho = 3$ g/cm^3. (a) Frictionless contacts. Rounded, concentric fold forms above fault in early stages. Fold becomes asymmetric at later stages. (b) Low but nonzero friction. Kink bands on limbs of fold. (c) High friction. Kink bands form on limbs of fold. (d) Bonded (no slip at layer contacts). Diffuse deformation. No buckling.

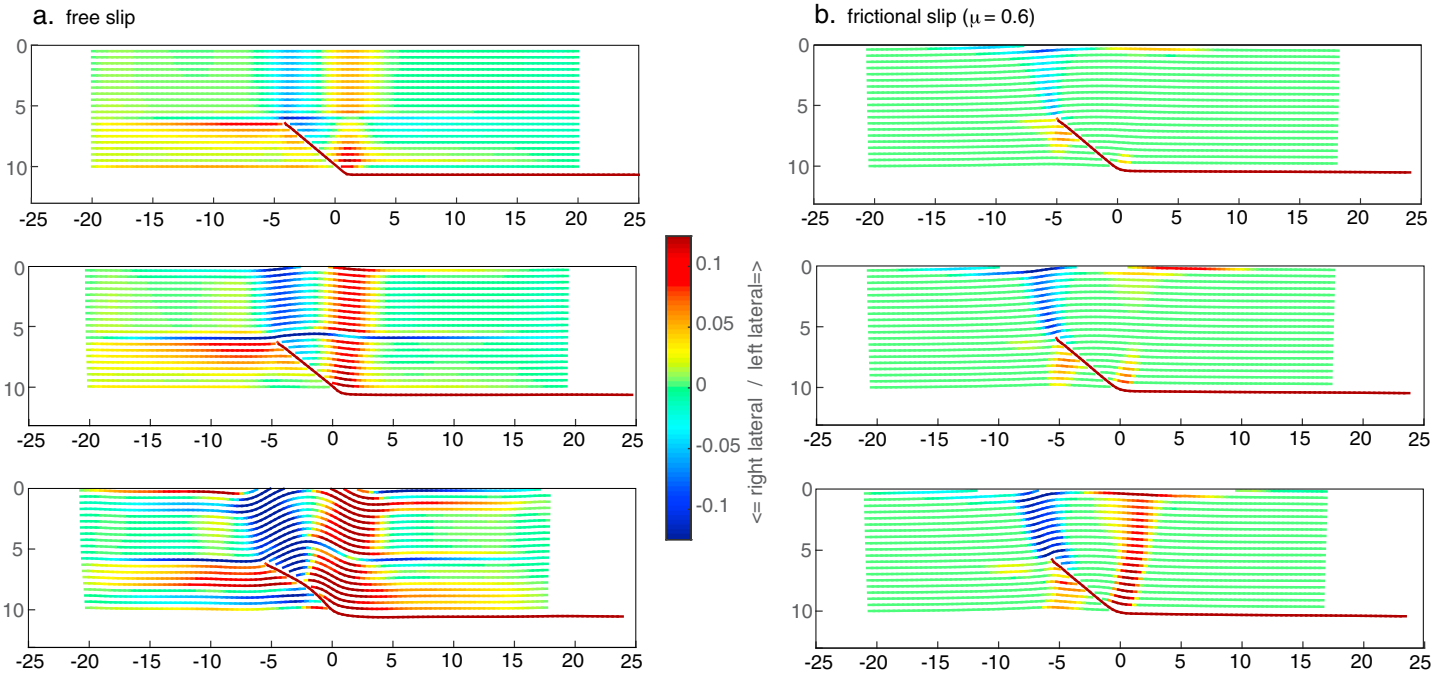

Figure 10. Role of friction on localizing fault slip. Color shows incremental slip in units of km for 1 km of imposed slip on the flat. (a) Free slip between layers (frictionless) leads to diffuse distribution of contact slip and concentric folding. (b) Frictional contacts lead to localized slip in kink bands.

6. Amplification of Folding by Buckling

In this section, we focus on the influence of buckling on the growth of fault-cored anticlines. We begin with a simple straight ramp fault with 40° fault dip that soles into a lower flat as illustrated in Figure 11a. We show the fold geometry after about 5 km of shortening above the flat for different layer thicknesses. The dashed markers indicate passive markers, and the solid lines indicate actual slip surfaces. Comparing the folds in layered media in Figures 11b–11d with the nonlayered medium in Figure 11a, it is clear that folding in the nonlayered material results in a broad, relatively low amplitude fold, whereas buckling of the multilayer leads to higher amplitude, more highly localized folds. Huang and Johnson (2016) showed that in this case, the amplification factor, which is the ratio of the amplitude of buckle folds to the amplitude of the passive fold (no layering), can range from modest values for thick layers to as much as about 4 for thinner layers. In this analysis, we compare the amplitude to slip ratio of the buckle folds to the amplitude to slip ratio assumed for a traditional kinematic model of fault-propagation folding (Figure 11c). Here the ratio is the peak incremental growth in fold amplitude during an increment of deformation divided by the average slip over the ramp fault. The amplitude to slip ratio is plotted as a function of slip on the flat in Figure 11b for the different layer thicknesses illustrated in Figure 11a. The horizontal dashed line in Figure 11b corresponds to the assumed ratio in the kinematic model. We see that for no layering, or relatively thick layers, the amplitude to slip ratio is lower than in the kinematic model. With thinner layers, the amplitude to slip ratio can increase to at least twice the ratio of the kinematic model after several increments of shortening.

It is also evident from Figure 11 that the ramp fault deforms along with the folded layering. The amount of deformation of the fault increases with the amount of buckle folding. Layers above and below the ramp fault buckle during deformation, and this buckling requires that the fault become deformed.

It is well known in the folding literature that the rate of fold growth is a function of layer thickness and wavelength of the deflection. M. A. Biot (1961) showed that an initially sinusoidal deflection with wavelength, l, of a stack of n stiff viscous layers of thickness, h, and viscosity, η, in a softer viscous medium of viscosity, η_1, increases exponentially in time under layer-parallel compressive stress, P. The amplitude of the sinusoidal deflection over time, t, is proportional to $e^{\alpha t}$, where

$$\alpha = \frac{P}{\frac{4\eta_1}{nhl} + \frac{1}{3}\eta h^2 l^2}. \tag{9}$$

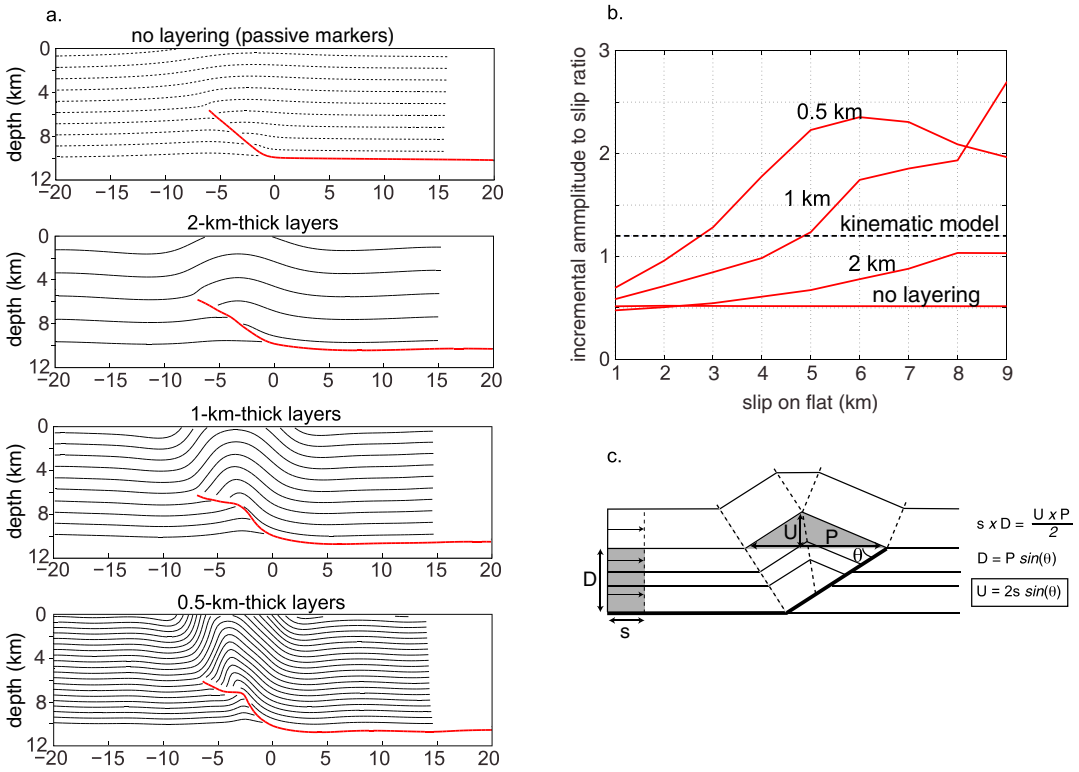

Figure 11. Amplification of folding of multilayer with free slip at contacts. (a) Fold form for different layer thicknesses after similar amounts of shortening. (b) Plot of the peak incremental growth in amplitude normalized by mean ramp fault slip with increasing slip on the flat for layer thicknesses illustrated in (a). Kinematic model refers to construction shown in (c). (c) Geometry of kinematic model construction. s = detachment slip, U = uplift, θ = fault dip, and D and P are distances as shown. Amplitude to slip ratio is U/s = 2sinθ.

As the softer medium approaches zero viscosity, there is no shear resistance between the competent layers,

$$\alpha \rightarrow \frac{3P}{\eta h^2 l^2}, \eta_1 \rightarrow 0. \tag{10}$$

Clearly from equation (10), the rate of fold growth increases with decreasing layer thickness, h, which is observed also in Figure 11. Identification of the wavelength that grows the fastest leads to the classical expression for the dominant wavelength, L_d,

$$L_d = 2\pi h \sqrt[3]{\frac{n\eta}{6\eta_1}}. \tag{11}$$

It is expected that this is the wavelength that will be mechanically selected to grow the fastest and dominate the folding process. We might also expect there to be a similar mechanical wavelength selection in buckling of fault-related folds; however, the relationship between wavelength and layer thickness is complicated by the existence of a fault. Figure 12 illustrates the joint influence of fault length and layer thickness on wavelength. Here we assume a purely elastic material (no viscous relaxation) with identical conditions to the simulations in Figure 11 (elastic shear modulus, $\mu = 10^9$ Pa, freeslip at layer contacts, and initial horizontal stress of $\sigma_{xx} = 10^7$ Pa). We impose 5 km of slip in each fold. It is clear from examination of Figure 12 that the wavelength of the folding is controlled by both fault length and layer thickness with longer wavelengths corresponding with longer ramp faults and thicker layers.

Figure 13 illustrates the exponential growth rate of folds shown in Figure 12. This is a plot of incremental increase in amplitude (not total amplitude) as a function of total slip on the flat for folds formed over different ramp lengths and different layer thicknesses. The slope of the curves is the instantaneous rate of growth of amplitude, which clearly increases with increased total slip until the latest stages of folding where this pattern breaks down and growth rate decreases.

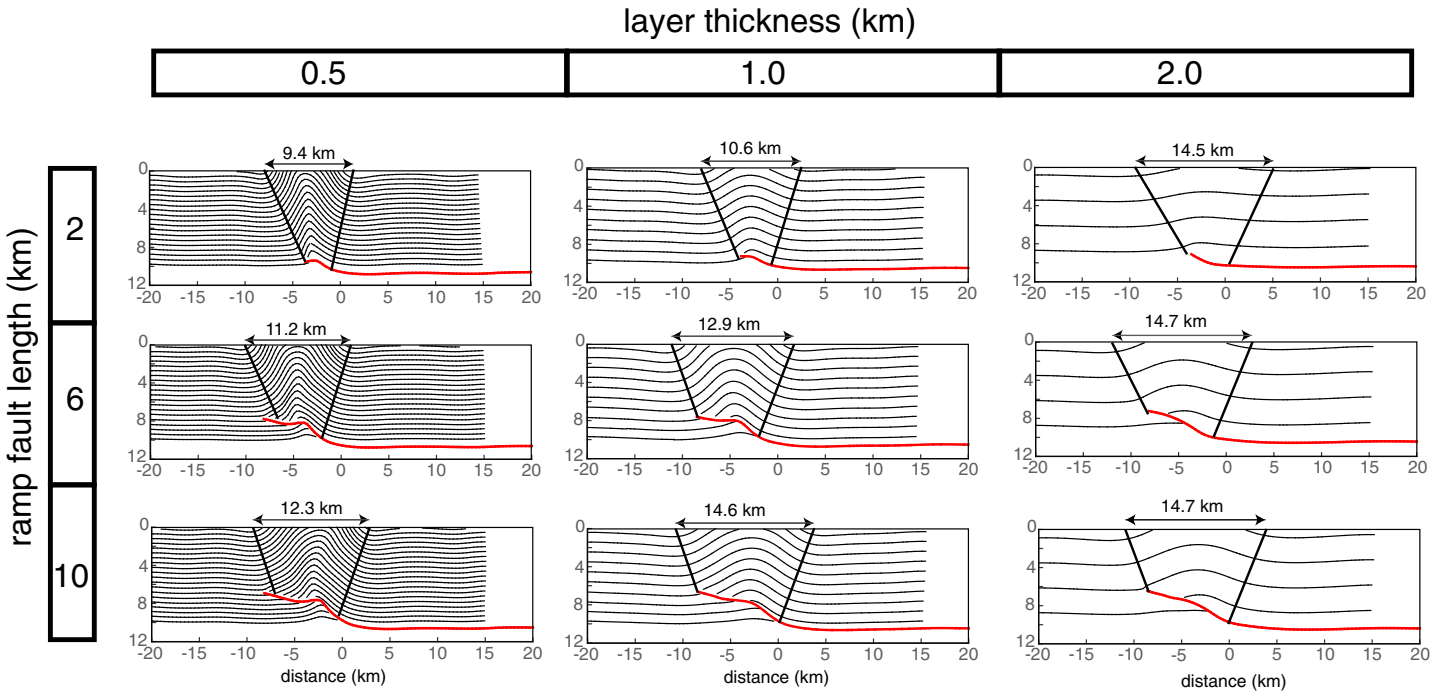

Figure 12. Influence of fault length and layer thickness on fold wavelength for freeslip at layer contacts. In all cases, $\mu = 10^9$ Pa, and $\sigma_{xx} = 10^7$ Pa. Initial fault ramp is straight with initial dip of 26°. Wavelength is controlled by both layer thickness and ramp length.

7. Influence of Fault Geometry on Fold Form

For the sake of making comparisons between simulations, up to this point, we have used a simple straight ramp fault geometry for all simulations. However, fault geometry is of course going to have an influence on fold geometry as well. Figure 14 shows the result of simulations with four different fault geometries with

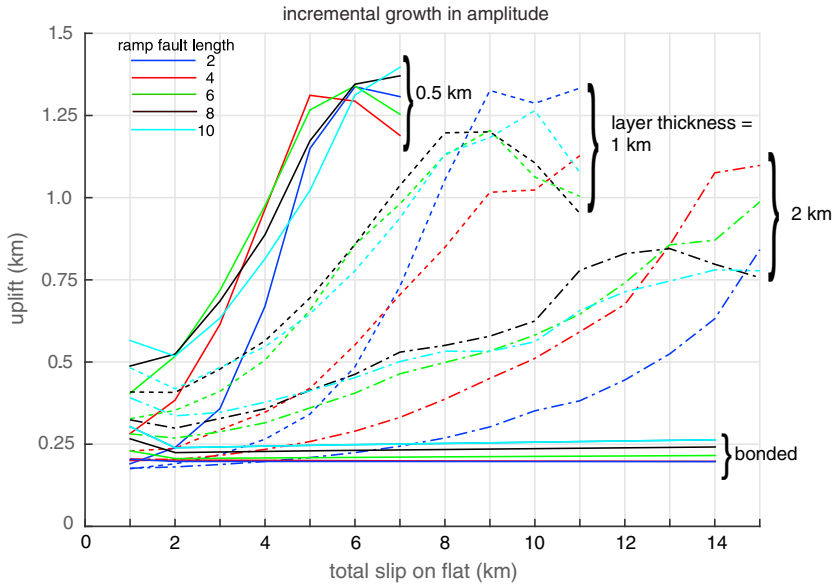

Figure 13. Incremental increase in amplitude as a function of slip on the flat for various ramp fault length and layer thicknesses. The slope of the curves is the instantaneous rate of growth of amplitude. The rate of amplification of the folding increases with total slip on the flat until the latest stages of folding.

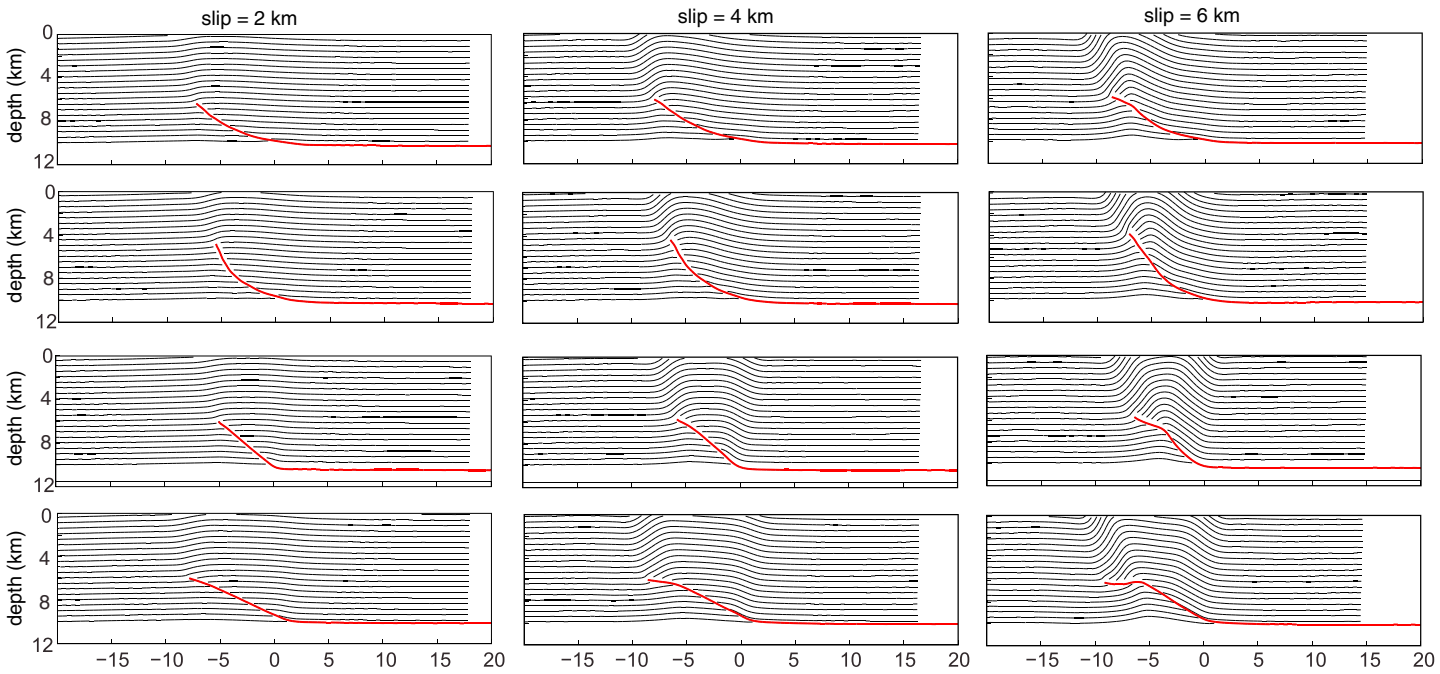

Figure 14. Influence of fault geometry on fold form. Fault geometry from top to bottom is low-angle listric fault, high-angle listric fault, high-angle straight fault, and low-angle straight fault. Conditions are the same for each of the four simulations (see text for details) except fault geometry. Total slip on the flat increases from left to right.

increasing slip on the flat shown from left to right in the figure. The other conditions are identical to those in Figure 12. The main result is that listric shaped ramps lead to highly asymmetric folds with a short forelimb and longer backlimb, whereas a straight ramp fault tends to produce more-nearly symmetric folds.

We examine fault-bend fold geometry in Figure 15 for free slip or bonded layer contacts with variable layer thickness. Figure 15a shows the fault-bend fold geometry at three stages of slip on the flat for relatively thin layering with free slip. Superimposed on the fold is the expected width and dip of forelimb and backlimb kink bands assuming the standard fault-bend fold geometry of Suppe (1983). After about 5 km of slip on the flat, the simulated fold geometry is very similar to the kinematic construction geometry. At earlier stages of folding, the simulated kink bands are slightly wider than in the kinematic construction. As the layering increases in thickness (Figures 15b–15d), the fold limbs become more rounded and wider and the geometry deviates more significantly from the idealized kinematic model.

8. Implications for Earthquake Studies

A major motivation for analysis of fault-related folds is assessment of earthquake hazard associated with the causative fault. Indeed, there is a large body of research centered on estimating fault slip and or earthquake recurrence using kinematic models of folding and associated growth strata (e.g., Dolan & Avouac, 2007, and references therein). However, if the buckling mechanism discussed in this paper is a significantly active mechanism in active fault-related folding, a potentially large component of fold growth might be attributed to buckling, in addition to slip on the underlying fault.

To examine this explicitly, we compute the on-fault and off-fault moment release for an anticline over a listric fault as illustrated in Figure 16a. The conditions are similar to previous simulations with elastic shear modulus, $\mu = 10^9$ Pa; layer contact friction $\mu_f = 0.4$; and initial horizontal stress of $\sigma_{xx} = 10^7$ Pa. Here we plot potency, which is moment divided by elastic shear modulus (slip times area). Figure 16b is a plot of cumulative moment/potency as a function of total slip on the flat for slip on the ramp fault (on-fault) and distributed slip at layer contacts (off-fault). During initial stages of folding (less than 5 km of slip) the on-fault moment is larger than the off-fault moment. However, at later stages (more than 5 km of shortening), the off-fault moment exceeds the on-fault moment and is more than twice the on-fault moment after 10 km of shortening. An

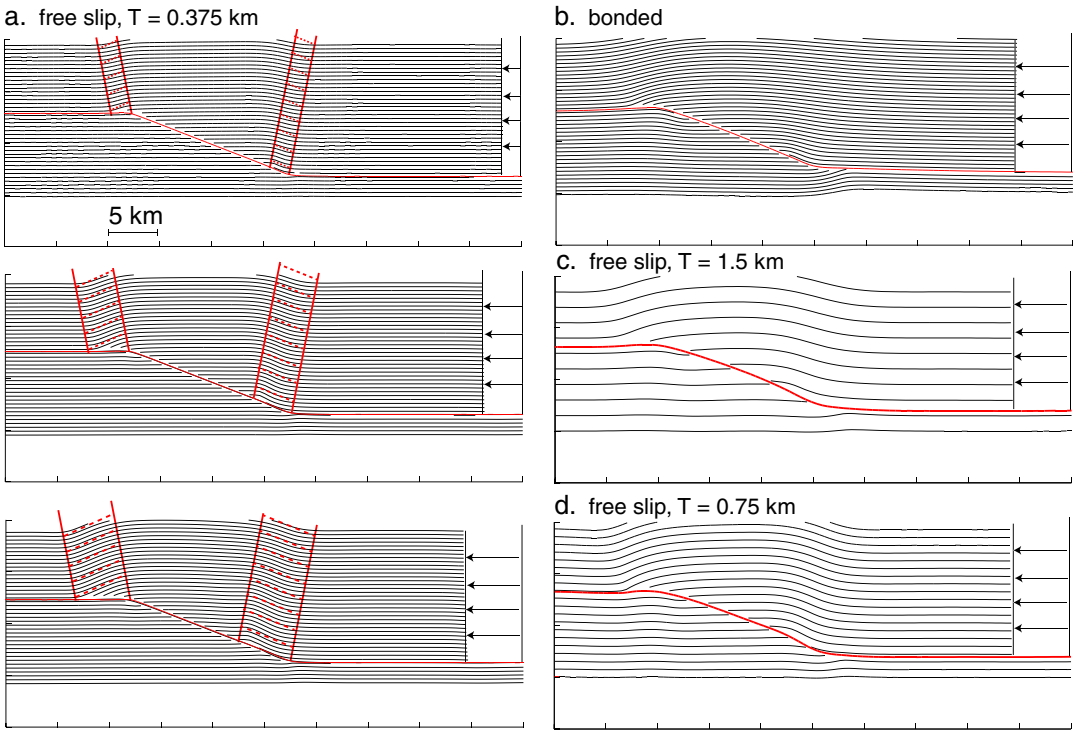

Figure 15. Fault-bend folding with variable layer thickness and (a, c, and d) free slip or (b) bonded contacts. The red construction lines are based on the classic fault-bend fold kinematic construction (e.g., Suppe, 1983).

interpretation of this result is that as the fold grows in amplitude, deformation is increasingly accommodated by buckle folding and decreasingly by fault slip. Figure 16c plots the incremental surface uplift normalized by incremental slip on the flat after 4, 6, 8, and 10 km of total shortening. This is the incremental vertical surface motion of the flat free surface, not taking into consideration erosion or deposition. Total incremental uplift is plotted with solid curves, and the incremental uplift contribution from slip on the ramp fault only (no bedding slip) is plotted with dashed curves. After about 5 km of shortening, half or more of the vertical displacement is due to distributed slip at layer contacts.

9. Discussion

This study has neglected several processes, at least, that may be important factors in fold evolution. We do not account for inelastic yielding within the viscoelastic layering. All inelasticity in these models occurs at contacts (as frictional slip). For sufficiently thin layers, relative to the wavelength of folding, this may not be a serious limitation because large stresses will not accumulate within thin layers. However, if the layering is thick enough, stresses may exceed the yield strength of rock and inelastic strain localization processes may become important. Previous mechanical analyses of fault-related folding have indeed shown that inelastic strain localization processes have a first-order influence on fold form in the absence of mechanical layering (e.g., Albertz & Lingrey, 2012; Cruz et al., 2017; Hughes et al., 2014).

To this point we have neglected deposition at the surface to facilitate the examination of the influence of other parameters on folding. While we do not systematically explore the geometry of growth strata or the influence of deposition rate on folding in this study, we can show that erosion and deposition do influence folding. Figure 17 compares folds produced under different surface conditions: no erosion or deposition (Figure 17a), complete erosion above the fixed free surface and no deposition (Figure 17b), and full erosion above the fixed free surface and deposition at a uniform rate of 0.25 km per 1 km of shortening (Figure 17c). The other parameters are the same for all simulations: $\mu_f = 0.4$, $\mu = 10^9$ Pa, and $\sigma_{xx} = 10^7$ Pa. A direct comparison of folding with and without erosion (and no deposition) is shown in Figure 17d. The influence of erosion

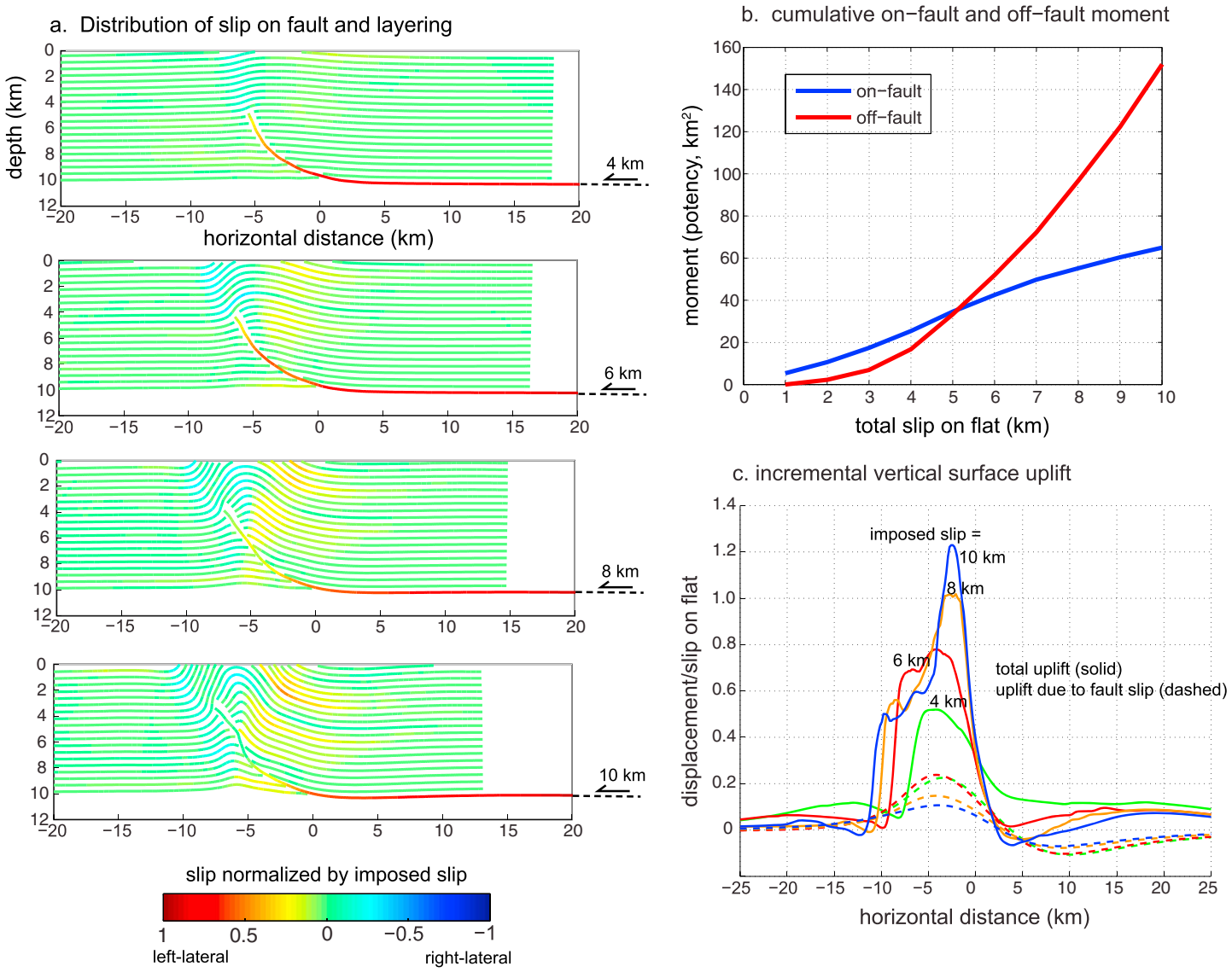

Figure 16. Implications for earthquakes. (a) Distribution of incremental slip along layering and fault (km). Each increment corresponds to 1 km of imposed slip on the flat. Slip on ramp fault decreases, and deformation becomes more distributed on layers as deformation progresses. Positive slip is left-lateral, and negative slip is right-lateral. (b) Plot of cumulative moment (potency) and off-fault moment (potency) as a function of total slip. On-fault moment decreases in rate somewhat with increasing slip, whereas off-fault moment increases in rate with increased slip. (c) Comparison of incremental surface uplift (solid lines, labeled total) and incremental uplift due only to fault slip (dashed lines) for different stages of folding. Colors represent incremental uplift at different amounts of total slip on the flat as noted.

on fold growth is dramatic. The fold with surface erosion is narrower with steeper limb dips and higher amplitude than the fold without erosion.

Finally, we have also neglect fault propagation to this point in this study. It was shown by Hardy and Ford (1997) and Allmendinger (1998), in the context of the trishear kinematic model, that the rate of propagation of the fault tip relative to the slip rate is an important factor on fold shape. Namely, the width of the shear zone ahead of the fault tip gets broader with lower rates of fault propagation. Fault propagation is likely to have an important influence on resultant buckle fold geometry, as well. As the fault tip propagates, the ramp fault lengthens, and as we show in Figure 12, the wavelength of the fold is controlled in part by the length of the ramp fault. In Figure 18 we compare the fold evolution for the case of propagating and nonpropagating faults. The conditions are similar to previous simulations with elastic shear

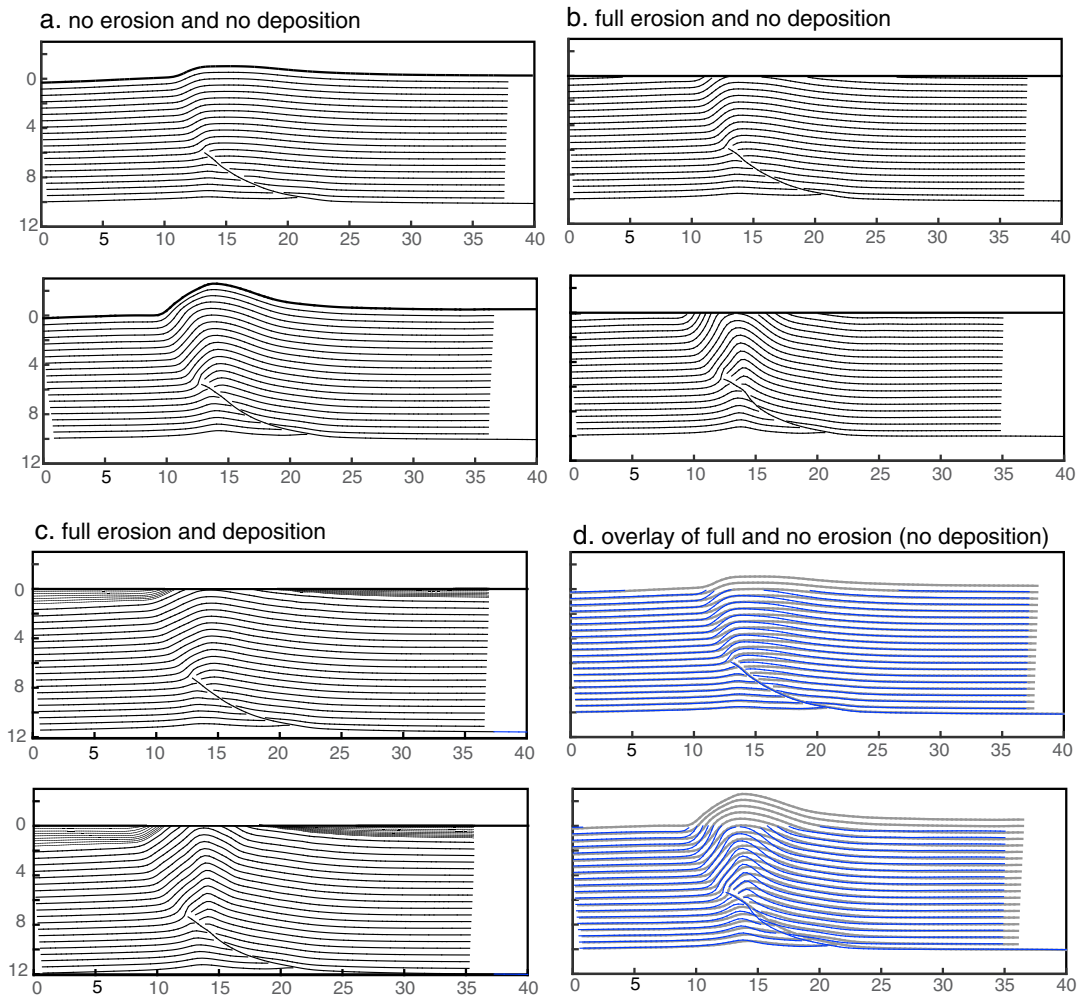

Figure 17. Influence of erosion and deposition on folding. (a) Folding with no deposition at the surface and no erosion of the free surface. (b) Folding without surface deposition and complete erosion (free surface remains flat). (c) Folding with uniform deposition rate and complete erosion of material above the free surface. Deposition rate is 0.25 km per 1 km of shortening. (d) Comparison of folds produced with and without erosion (no deposition). The blue lines show fold with complete erosion, and the gray lines show folded layers with no erosion.

modulus, $\mu = 10^9$ Pa; initial horizontal stress of $\sigma_{xx} = 10^7$ Pa; and contact friction of $\mu_f = 0.2$. To propagate the fault in Figure 18a, we kinematically impose incremental lengthening of the ramp fault. We extend the tip of the ramp fault upward along the dip of the fault by 1.5 km for every 1 km of imposed slip on the flat. Figure 18b shows a simulation under identical conditions except that there is no fault propagation and the fault ramp length is chosen to be the same length as the final ramp length in Figure 18a. Comparing these two simulations, we deduce that the primary effect of the propagating fault in this simulation is progressive widening of the fold with increased shortening and increased ramp length. However, at the final stage of folding, the fold produced over the propagating fault is narrower than the fold produced by the nonpropagating fault. This narrower fold appears to be a result of buckling of an initially narrower deflection in the earlier stages of folding over the shorter fault ramp. We further note that the nonpropagating ramp fault in our simulations becomes deformed during folding. There is a tendency for the upper part of the ramp fault to bend toward horizontal as the surrounding strata are folded. There is less distortion of the ramp fault geometry in the case of the propagating fault. It seems possible that a propagating fault in nature would tend to be less highly deformed by folding of the surrounding strata; however, we cannot investigate this fully because here we have kinematically

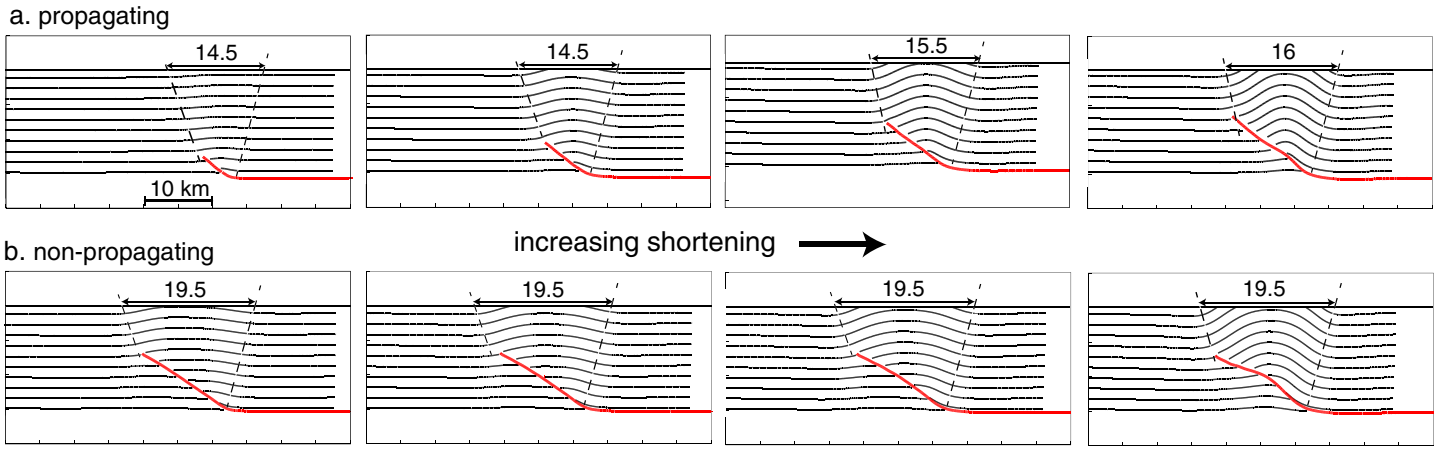

Figure 18. Influence of fault propagation on fold form. The dashed lines show axial traces, and the arrows denote width of fold at the free surface. For both simulations, $\mu = 10^9$ Pa, $\sigma_{xx} = 10^7$ Pa, and $\mu_f = 0.2$. (a) Fault tip is propagated kinematically by lengthening the ramp fault 1.5 km per 1 km of slip on the flat. (b) No fault propagation. Note that the wavelength of the fold does not change with fold evolution while the fold in (a) widens as the fault propagates.

imposed the propagation path of the fault tip. Future studies would benefit from examining this issue with mechanical constraints on fault tip propagation.

10. Conclusions

In this study, we have constructed a boundary element model of fault-related folding consisting of viscoelastic layers in frictional contact embedded with a fault. We ran a number of numerical simulations to examine the influence of various factors on the rate of fold growth and the resulting fold geometry. We have shown that the strength of bedding contacts, the thickness and stiffness of layering, and fault geometry all contribute significantly to the resulting fold form.

We examined the influence of elastic and viscoelastic properties on faulting. We find that effective elastic stiffness of layering influences the degree to which kink bands form on the limbs of folds. As illustrated in Figure 6, stiffer layers lead to more rounded fold forms whereas softer layers lead to sharp-hinged, flat-topped folds with kink bands forming the fold limbs. The rate of viscous dissipation could be an important factor on the ability for flexural slip to occur. As shown in Figure 7, if the characteristic relaxation time of viscous flow within layering is fast relative to the loading rate, dissipation of stresses by viscous flow inhibits flexural slip folding. As the relaxation time increases relative to the loading rate, flexural slip is enhanced and amplification of folding by buckling dominates the folding process.

Contact strength has a first-order influence on fold form, consistent with previous laboratory and theoretical studies of free folds. As illustrated in Figures 8, 9, and 10, low contact strength leads to rounded, concentric fold forms whereas high contact strength leads to kink bands on the limbs of folds. With low frictional contact strength, the amplitude a fault-cored flexural slip fold can grow 4–5 times faster than a fold without layering as shown in Figure 11.

We show that fault geometry also has an important influence on fold form. Straight ramp faults tend to produce symmetric folds and listric faults tend to produce asymmetric folds (Figure 14). The width of anticlines over blind faults is controlled by the length of the underlying ramp fault as well as the layer thickness as shown in Figure 12. If bedding is sufficiently thin, the geometry of fault-bend fold geometry associated with ramp fault connecting upper and lower flats is similar to the classic kinematic construction as illustrated in Figure 15.

Finally, we examined how fold growth evolves over time and find that the rate of fold growth increases with time under steady loading conditions as demonstrated in Figure 13 and as expected from elementary folding theory (Biot, 1961). The proportion of on-fault versus off-fault moment release evolves over time as the fold grows (Figure 16). At early stages of folding the majority of moment release is due to fault slip, but at later stages of folding more moment is released through distributed slip at layer contacts.

Acknowledgments
The author would like to thank Arvid M. Johnson for conversations on this topic as well as Rick Allmendinger and the Associate Editor for helpful comments. All data (output model runs) are available in the figures in this manuscript.

References

Albertz, M., & Lingrey, S. (2012). Critical state finite element models of contractional fault-related folding: Part 1. Structural analysis. *Tectonophysics*, *576*, 133–149.

Allmendinger, R. W. (1998). Inverse and forward numerical modeling of trishear fault-propagation folds. *Tectonics*, *17*(4), 640–656. https://doi.org/10.1029/98TC01907

Allmendinger, R. W., & Shaw, J. H. (2000). Estimation of fault propagation distance from fold shape: Implications for earthquake hazard assessment. *Geology*, *28*(12), 1099–1102. https://doi.org/10.1130/0091-7613(2000)28%3C1099:EOFPDF%3E2.0.CO;2

Belabbès, S., Meghraoui, M., Çakir, Z., & Bouhadad, Y. (2009). InSAR analysis of a blind thrust rupture and related active folding: The 1999 Ain Temouchent earthquake (M w 5.7, Algeria) case study. *Journal of Seismology*, *13*(4), 421–432. https://doi.org/10.1007/s10950-008-9135-x

Berger, P., & Johnson, A. M. (1982). Folding of passive layers and forms of minor structures near terminations of blind thrust faults—Application to the central Appalachian blind thrust. *Journal of Structural Geology*, *4*(3), 343–353. https://doi.org/10.1016/0191-8141(82)90018-9

Biot, M. A. (1961). Theory of folding of stratified viscoelastic media and its implications in tectonics and orogenesis. *Geological Society of America Bulletin*, *72*(11), 1595–1620. https://doi.org/10.1130/0016-7606(1961)72%5B1595:TOFOSV%5D2.0.CO;2

Biot, M. (1964). Theory of internal buckling of a confined multilayered structure. *Geological Society of America Bulletin*, *75*(6), 563–568. https://doi.org/10.1130/0016-7606(1964)75%5B563:TOIBOA%5D2.0.CO;2

Bonanno, E., Bonini, L., Basili, R., Toscani, G., & Seno, S. (2017). How do horizontal, frictional discontinuities affect reverse fault-propagation folding? *Journal of Structural Geology*, *102*, 147–167. https://doi.org/10.1016/j.jsg.2017.08.001

Brandes, C., & Tanner, D. C. (2014). Fault-related folding: A review of kinematic models and their application. *Earth-Science Reviews*, *138*, 352–370. https://doi.org/10.1016/j.earscirev.2014.06.008

Cardozo, N., Bhalla, K., Zehnder, A. T., & Allmendinger, R. W. (2003). Mechanical models of fault propagation folds and comparison to the trishear kinematic model. *Journal of Structural Geology*, *25*(1), 1–18. https://doi.org/10.1016/S0191-8141(02)00013-5

Cardozo, N., Allmendinger, R. W., & Morgan, J. K. (2005). Influence of mechanical stratigraphy and initial stress state on the formation of two fault propagation folds. *Journal of Structural Geology*, *27*(11), 1954–1972. https://doi.org/10.1016/j.jsg.2005.06.003

Chapple, W. M. (1969). Fold shape and rheology: The folding of an isolated viscous-plastic layer. *Tectonophysics*, *7*(2), 97–116. https://doi.org/10.1016/0040-1951(69)90001-8

Chester, J., & Chester, F. (1990). Fault-propagation folds above thrusts with constant dip. *Journal of Structural Geology*, *12*(7), 903–910. https://doi.org/10.1016/0191-8141(90)90063-5

Cobbold, P. (1976). Fold shapes as functions of progressive strain. *Philosophical Transactions of the Royal Society of London A: Mathematical, Physical and Engineering Sciences*, *283*(1312), 129–138. https://doi.org/10.1098/rsta.1976.0073

Cooke, M., & Pollard, D. (1997). Bedding-plane slip in initial stages of fault-related folding. *Journal of Structural Geology*, *19*(3-4), 567–581. https://doi.org/10.1016/S0191-8141(96)00097-1

Crouch, S. L. & Starfield, A. M. (1983). *Boundary element methods in solid mechanics*. London: George Allen & Unwin.

Cruz, L., Nevitt, J., Seixas, G., & Hilley, G. (2017). What do kinematic models imply about the constitutive properties of rocks deformed in flat-ramp-flat folds? *Geophysical Research Letters*, *44*, 9581–9588. https://doi.org/10.1002/2017GL074397

Dolan, J. F., & Avouac, J. P. (2007). Introduction to special section: Active fault-related folding: Structural evolution, geomorphologic expression, paleoseismology, and seismic hazards. *Journal of Geophysical Research*, *112*, B03S01. https://doi.org/10.1029/2007JB004952

Duebendorfer, E. M., & Meyer, K. L. (2002). Penetrative strain at shallow crustal levels: The role of pressure solution in accommodating regional shortening strain, Ventura basin, western Transverse ranges, California. *Special Paper of the Geological Society of America*, *365*, 295–314. https://doi.org/10.1130/0-8137-2365-5.295

Erslev, E. A. (1991). Trishear fault-propagation folding. *Geology*, *19*(6), 617–620. https://doi.org/10.1130/0091-7613(1991)019%3C0617:TFPF%3E2.3.CO;2

Finch, E., Hardy, S., & Gawthorpe, R. (2003). Discrete element modelling of contractional fault-propagation folding above rigid basement fault blocks. *Journal of Structural Geology*, *25*(4), 515–528. https://doi.org/10.1016/S0191-8141(02)00053-6

Fletcher, R. C. (1977). Folding of a single viscous layer: Exact infinitesimal-amplitude solution. *Tectonophysics*, *39*(4), 593–606. https://doi.org/10.1016/0040-1951(77)90155-X

Gonzalez-Mieres, R., & Suppe, J. (2006). Relief and shortening in detachment folds. *Journal of Structural Geology*, *28*(10), 1785–1807. https://doi.org/10.1016/j.jsg.2006.07.001

Grant, L. B., Mueller, K. J., Gath, E. M., Cheng, H., Edwards, R. L., Munro, R., & Kennedy, G. L. (1999). Late Quaternary uplift and earthquake potential of the San Joaquin Hills, southern Los Angeles basin, California. *Geology*, *27*(11), 1031–1034. https://doi.org/10.1130/0091-7613(1999)027%3C1031:LQUAEP%3E2.3.CO;2

Gratier, J., & Gamond, J. (1990). Transition between seismic and aseismic deformation in the upper crust. *Geological Society, London, Special Publications*, *54*(1), 461–473. https://doi.org/10.1144/GSL.SP.1990.054.01.42

Gratier, J.-P., Renard, F., & Labaume, P. (1999). How pressure solution creep and fracturing processes interact in the upper crust to make it behave in both a brittle and viscous manner. *Journal of Structural Geology*, *21*(8-9), 1189–1197. https://doi.org/10.1016/S0191-8141(99)00035-8

Guzofski, C. A., Shaw, J. H., Lin, G., & Shearer, P. M. (2007). Seismically active wedge structure beneath the Coalinga anticline, San Joaquin basin, California. *Journal of Geophysical Research*, *112*, B03S05. https://doi.org/10.1029/2006JB004465

Hardy, S., & Ford, M. (1997). Numerical modeling of trishear fault propagation folding. *Tectonics*, *16*(5), 841–854. https://doi.org/10.1029/97TC01171

Hogan, J. P., & Dunne, W. M. (2001). Calculation of shortening due to outcrop-scale deformation and its relation to regional deformation patterns. *Journal of Structural Geology*, *23*(10), 1507–1529. https://doi.org/10.1016/S0191-8141(01)00016-5

Honea, E., & Johnson, A. M. (1976). A theory of concentric, kink and sinusoidal folding and of monoclinal flexuring of compressible, elastic multilayers: IV. Development of sinusoidal and kink folds in multilayers confined by rigid boundaries. *Tectonophysics*, *30*(3–4), 197–239. https://doi.org/10.1016/0040-1951(76)90187-6

Huang, W. J., & Johnson, K. M. (2012). Strain accumulation across strike-slip faults: Investigation of the influence of laterally varying lithospheric properties. *Journal of Geophysical Research*, *117*, B09407. https://doi.org/10.1029/2012JB009424

Huang, W.-J., & Johnson, K. M. (2016). A fault-cored anticline boundary element model incorporating the combined fault slip and buckling mechanisms. *Terrestrial, Atmospheric & Oceanic Sciences*, *27*(1), 073. https://doi.org/10.3319/TAO.2015.06.18.01(TT)

Hughes, A. N., Benesh, N. P., & Shaw, J. H. (2014). Factors that control the development of fault-bend versus fault-propagation folds: Insights from mechanical models based on the discrete element method (DEM). *Journal of Structural Geology*, *68*, 121–141. https://doi.org/10.1016/j.jsg.2014.09.009

Ishiyama, T., Mueller, K., Togo, M., Okada, A., & Takemura, K. (2004). Geomorphology, kinematic history, and earthquake behavior of the active Kuwana wedge thrust anticline, central Japan. *Journal of Geophysical Research*, *109*, B12408. https://doi.org/10.1029/2003JB002547

Johnson, A. M., & Berger, P. (1989). Kinematics of fault-bend folding. *Engineering Geology*, *27*(1–4), 181–200. https://doi.org/10.1016/0013-7952(89)90033-1

Johnson, A. M., & Fletcher, R. C. (1994). *Folding of viscous layers: Mechanical analysis and interpretation of structures in deformed rock*. New York: Columbia University Press.

Johnson, K. M., & Johnson, A. M. (2002). Mechanical analysis of the geometry of forced-folds. *Journal of Structural Geology*, *24*(3), 401–410. https://doi.org/10.1016/S0191-8141(01)00085-2

Johnson, A. M., & Pfaff, V. J. (1989). Parallel, similar and constrained folds. *Engineering Geology*, *27*(1–4), 115–180. https://doi.org/10.1016/0013-7952(89)90032-X

Kemeny, J., & Cook, N. (1986). *Effective moduli, non-linear deformation and strength of a cracked elastic solid*. Paper presented at the International Journal of Rock Mechanics and Mining Sciences & Geomechanics Abstracts.

Kilsdonk, B., & Fletcher, R. C. (1989). An analytical model of hanging-wall and footwall deformation at ramps on normal and thrust faults. *Tectonophysics*, *163*(1–2), 153–168. https://doi.org/10.1016/0040-1951(89)90123-6

Mancktelow, N. (1999). Finite-element modelling of single-layer folding in elasto-viscous materials: The effect of initial perturbation geometry. *Journal of Structural Geology*, *21*(2), 161–177. https://doi.org/10.1016/S0191-8141(98)00102-3

McEwen, T. (1978). Diffusional mass transfer processes in pitted pebble conglomerates. *Contributions to Mineralogy and Petrology*, *67*(4), 405–415. https://doi.org/10.1007/BF00383300

Mitra, G. (1994). Strain variation in thrust sheets across the Sevier fold-and-thrust belt (Idaho-Utah-Wyoming): Implications for section restoration and wedge taper evolution. *Journal of Structural Geology*, *16*(4), 585–602. https://doi.org/10.1016/0191-8141(94)90099-X

Niño, F., Philip, H., & Chéry, J. (1998). The role of bed-parallel slip in the formation of blind thrust faults. *Journal of Structural Geology*, *20*(5), 503–516. https://doi.org/10.1016/S0191-8141(97)00102-8

Nissen, E., Ghorashi, M., Jackson, J., Parsons, B., & Talebian, M. (2007). The 2005 Qeshm Island earthquake (Iran)—A link between buried reverse faulting and surface folding in the Zagros Simply Folded Belt? *Geophysical Journal International*, *171*(1), 326–338. https://doi.org/10.1111/j.1365-246X.2007.03514.x

Patton, T. L., & Fletcher, R. C. (1995). Mathematical block-motion model for deformation of a layer above a buried fault of arbitrary dip and sense of slip. *Journal of Structural Geology*, *17*(10), 1455–1472. https://doi.org/10.1016/0191-8141(95)00034-B

Pezzo, G., Boncori, J. P. M., Tolomei, C., Salvi, S., Atzori, S., Antonioli, A., et al. (2013). Coseismic deformation and source modeling of the May 2012 Emilia (Northern Italy) earthquakes. *Seismological Research Letters*, *84*(4), 645–655. https://doi.org/10.1785/0220120171

Pfaff, V. J., & Johnson, A. M. (1989). Opposite senses of fold asymmetry. *Engineering Geology*, *27*(1–4), 3–38. https://doi.org/10.1016/0013-7952(89)90030-6

Poblet, J., & McClay, K. (1996). Geometry and kinematics of single-layer detachment folds. *AAPG Bulletin*, *80*(7), 1085–1109.

Reches, Z. e., & Johnson, A. M. (1976). A theory of concentric, kink and sinusoidal folding and of monoclinal flexuring of compressible, elastic multilayers: VI. Asymmetric folding and monoclinal kinking. *Tectonophysics*, *35*(4), 295–334. https://doi.org/10.1016/0040-1951(76)90074-3

Reches, Z. e., & Johnson, A. M. (1978). Development of monoclines: Part II. Theoretical analysis of monoclines. *Geological Society of America Memoirs*, *151*, 273–312. https://doi.org/10.1130/MEM151-p273

Rutter, E., & Elliott, D. (1976). The kinetics of rock deformation by pressure solution. *Philosophical Transactions for the Royal Society of London. Series A, Mathematical and Physical Sciences*, *283*(1312), 203–219. https://doi.org/10.1098/rsta.1976.0079

Sanz, P. F., Pollard, D. D., Allwardt, P. F., & Borja, R. I. (2008). Mechanical models of fracture reactivation and slip on bedding surfaces during folding of the asymmetric anticline at Sheep Mountain, Wyoming. *Journal of Structural Geology*, *30*(9), 1177–1191. https://doi.org/10.1016/j.jsg.2008.06.002

Savage, H. M., & Cooke, M. L. (2003). Can flat-ramp-flat fault geometry be inferred from fold shape?: A comparison of kinematic and mechanical folds. *Journal of Structural Geology*, *25*(12), 2023–2034. https://doi.org/10.1016/S0191-8141(03)00080-4

Segall, P. (2010). *Earthquake and volcano deformation*. Princeton, NJ: Princeton University Press. https://doi.org/10.1515/9781400833856

Shackleton, J. R., & Cooke, M. L. (2007). Is plane strain a valid assumption in non-cylindrical fault-cored folds? *Journal of Structural Geology*, *29*(7), 1229–1240. https://doi.org/10.1016/j.jsg.2007.03.011

Shaw, J. H., & Suppe, J. (1994). Active faulting and growth folding in the eastern Santa Barbara Channel, California. *Geological Society of America Bulletin*, *106*(5), 607–626.

Shaw, J. H., Plesch, A., Dolan, J. F., Pratt, T. L., & Fiore, P. (2002). Puente Hills blind-thrust system, Los Angeles, California. *Bulletin of the Seismological Society of America*, *92*(8), 2946–2960. https://doi.org/10.1785/0120010291

Stein, R. S., & Ekström, G. (1992). Seismicity and geometry of a 110-km-long blind thrust fault 2. Synthesis of the 1982–1985 California earthquake sequence. *Journal of Geophysical Research*, *97*(B4), 4865–4883. https://doi.org/10.1029/91JB02847

Stein, R. S., & King, G. C. (1984). Seismic potential revealed by surface folding: 1983 Coalinga, California, earthquake. *Science*, *224*(4651), 869–872. https://doi.org/10.1126/science.224.4651.869

Sugiyama, Y., Mizuno, K., Nanayama, F., Sugai, T., Yokota, H., Hosoya, T., et al. (2003). Study of blind thrust faults underlying Tokyo and Osaka urban areas using a combination of high-resolution seismic reflection profiling and continuous coring. *Annals of Geophysics*, *46*(5), 1071–1085.

Suppe, J. (1983). Geometry and kinematics of fault-bend folding. *American Journal of Science*, *283*(7), 684–721. https://doi.org/10.2475/ajs.283.7.684

Suppe, J., & Medwedeff, D. A. (1990). Geometry and kinematics of fault-propagation folding. *Eclogae Geologicae Helvetiae*, *83*(3), 409–454.

Tizzani, P., Castaldo, R., Solaro, G., Pepe, S., Bonano, M., Casu, F., et al. (2013). New insights into the 2012 Emilia (Italy) seismic sequence through advanced numerical modeling of ground deformation InSAR measurements. *Geophysical Research Letters*, *40*, 1971–1977. https://doi.org/10.1002/grl.50290

Veloza, G., Taylor, M., Mora, A., & Gosse, J. (2015). Active mountain building along the eastern Colombian Subandes: A folding history from deformed terraces across the Tame anticline, Llanos Basin. *Geological Society of America Bulletin*, *127*(9–10), 1155–1173. https://doi.org/10.1130/B31168.1

Wickham, J. (1995). Fault displacement-gradient folds and the structure at Lost Hills, California (USA). *Journal of Structural Geology*, *17*(9), 1293–1302. https://doi.org/10.1016/0191-8141(95)00029-D

Wiltschko, D. (1979). A mechanical model for thrust sheet deformation at a ramp. *Journal of Geophysical Research*, *84*(B3), 1091–1104. https://doi.org/10.1029/JB084iB03p01091

Yonkee, A., & Weil, A. B. (2010). Reconstructing the kinematic evolution of curved mountain belts: Internal strain patterns in the Wyoming salient, Sevier thrust belt, USA. *Geological Society of America Bulletin*, *122*(1–2), 24–49. https://doi.org/10.1130/B26484.1

Yue, L.-F., Suppe, J., & Hung, J.-H. (2011). Two contrasting kinematic styles of active folding above thrust ramps, western Taiwan. In K. McClay, J. H. Shaw, & J. Suppe (Eds.), *Thrust Fault-Related Folding*, *AAPG Memoir 94* (pp. 153–186). Tulsa, OK: American Association of Petroleum Geologists.